China Geology 7 (2024) 730−746

China Geology

Journal homepage: http://chinageology.cgs.cn
https://www.sciencedirect.com/journal/china-geology

In situ U-Pb dating and trace elements of magmatic rutile from Mujicun Cu-Mo deposit, North China Craton: Insights into porphyry mineralization

Fan Yang[a, b,*], Jing-wen Mao[a], Wei-dong Ren[b], Jia-run Tu[c], Gilby Jepson[d], Si-yuan Meng[e], Zhi-min Wang[e]

[a] *MNR Key Laboratory of Metallogeny and Mineral Assessment, Institute of Mineral Resources, Chinese Academy of Geological Sciences, Beijing* 100037, *China*
[b] *Key Laboratory of Mineral Resources in Western China (Gansu Province), School of Earth Sciences, Lanzhou University, Lanzhou* 730000, *China*
[c] *Tianjin Center, China Geological Survey, Tianjin* 300170, *China*
[d] *Department of Geosciences, University of Arizona, Tucson AZ*85721, *USA*
[e] *Hebei Geological Engineering Exploration Institute, Baoding* 071051, *China*

ARTICLE INFO

Article history:
Received 27 February 2023
Received in revised form 1 May 2023
Accepted 9 June 2023
Available online 28 June 2023

Keywords:
Rutile U-Pb geochronology
Rutile geochemistry
Intra-continental porphyry mineralization
Paleo-Pacific slab subduction
Tectonic evolution
Magma source
Ore-forming age
Mujicun Cu-Mo deposit
Mineral exploration engineering
North China Craton

ABSTRACT

Porphyry Cu (Mo-Au) deposit is one of the most important types of copper deposit and usually formed under magmatic arc-related settings, whilst the Mujicun porphyry Cu-Mo deposit in North China Craton uncommonly generated within intra-continental settings. Although previous studies have focused on the age, origin and ore genesis of the Mujicun deposit, the ore-forming age, magma source and tectonic evolution remain controversial. Here, this study targeted rutile (TiO_2) in the ore-hosting diorite porphyry from the Mujicun Cu-Mo deposit to conduct *in situ* U-Pb dating and trace element composition studies, with major views to determine the timing and magma evolution and to provide new insights into porphyry Cu-Mo metallogeny. Rutile trace element data show flat-like REE patterns characterized by relatively enrichment LREEs and depleted HREEs, which could be identified as magmatic rutile. Rutile U-Pb dating yields lower intercept ages of 139.3–138.4 Ma, interpreted as post magmatic cooling timing below about 500°C, which are consistent or slightly postdate with the published zircon U-Pb ages of diorite porphyry (144.1–141.7 Ma) and skarn (146.2 Ma; 139.9 Ma) as well as the molybdenite Re-Os ages of molybdenum ores (144.8–140.0 Ma). Given that the overlap between the closure temperature of rutile U-Pb system and ore-forming temperature of the Mujicun deposit, this study suggests that the ore-forming ages of the Mujicun deposit can be constrained at 139.3–138.4 Ma, with temporal links to the late large-scale granitic magmatism at 138–126 Ma in the Taihang Orogen. Based on the Mg and Al contents in rutile, the magma of ore-hosting diorite porphyry was suggested to be derived from crust-mantle mixing components. In conjunction with previous studies in Taihang Orogen, this study proposes that the far-field effect and the rollback of the subducting Paleo-Pacific slab triggered lithospheric extension, asthenosphere upwelling, crust-mantle interaction and thermo-mechanical erosion, which jointly facilitated the formation of dioritic magmas during the Early Cretaceous. Subsequently, the dioritic magmas carrying crust-mantle mixing metallic materials were emplaced and precipitated at shallow positions along NNE-trending ore-controlling faults, eventually resulting in the formation of the Mujicun Cu-Mo deposit within an intra-continental extensional setting.

1. Introduction

Porphyry Cu (Mo-Au) deposit is an important type of copper deposit, which is also the major source for Cu, Mo and Au resources (Cannell J et al., 2005; Mao JW et al., 2018). Published studies suggested that most of porphyry Cu polymetallic deposits formed under arc-related settings and are closely correlated with calc-alkali magma (Sillitoe RH, 1972, 2010), but a few porphyry Cu deposits could also be generated within intra-continental and continental collision settings (Hou ZQ et al., 2003, 2009; Mao J et al., 2014; Gao YF et al., 2013; Lin B et al., 2023). The majority of studies have revealed that the formation of continental porphyry Cu deposits is closely correlated with continent-continent collisional orogen and/or the margin of craton related to plate subduction (Rui ZY et al., 2003; Bertrand G et al., 2014;

* Corresponding author: *E-mail address*: fanyang@lzu.edu.cn (Fan Yang).

Literary editor: Li-qiong Jia
doi:10.31035/cg2023038
2096-5192/© 2024 China Geology Editorial Office.

Asadi S et al., 2014; Yang ZM et al., 2016; Richards JP, 2022; Yang HH et al., 2022; Li WC et al., 2022; Zhang S et al., 2023). However, there are still shortage of studies to probe into the formation processes of intra-continental porphyry Cu deposits.

The Mujicun deposit in the Taihang tectonic-magmatic-metallogenic belt, central North China Craton (NCC) (Fig. 1) is a representative intra-continental porphyry Cu-Mo deposit (Gao YF et al., 2013; Dong GC et al., 2013), which is also the largest porphyry Cu deposit in the North Taihang Orogen and is mainly hosted in diorite porphyry, with proven reserves of 98.1 Mt Cu and 3.1 Mt Mo (Chen C et al., 2015). Previous studies determined the ore-forming ages of the Mujicun Cu-Mo deposit at 145.5–138.5 Ma (Gao YF et al., 2011; Chen C et al., 2013; Dong GC et al., 2013; Shen ZC et al., 2015), the emplacement ages of the ore-hosting diorite porphyry at 144.1–141.7 Ma (Gao YF et al., 2013, 2011; Dong GC et al., 2013; Shen JF et al., 2015), and the timing of formation of andesite (150.5–140.8 Ma; Gao YC et al., 2011) and epidote skarn (146.2–139.9 Ma; Dong GC et al., 2013) in this deposit, which together show a temporal link between the Cu-Mo mineralization and shallow (sub-) volcanism at 151–138 Ma. The Taihang Orogen subsequently developed large-scale granitic magmatism at 138–126 Ma (Chen B et al., 2005), but a few studies argued that this period of magmatism did not have genetic relationships with the Mujicun Cu-Mo mineralization (Gao YF et al., 2011), which show some conflicts with the published molybdenite Re-Os model age of 138.5 ± 1.9 Ma in the Mujicun deposit (Dong GC et al., 2013). Moreover, the magma and ore-forming material sources of the Mujicun Cu-Mo deposit are also controversial. Some studies supported that the magma and ore-forming materials of the Mujicun deposit are sourced from the interaction of both partial melting of ancient lower crust and contaminated mantle compositions (Dong GC et al., 2013; Qu K et al., 2014). Whereas other studies claimed that the magma was derived from partial melting of enriched mantle, which then underwent crustal assimilation and contamination and fractional crystallization during magma ascension (Gao YF et al., 2013; Shen ZC et al., 2015; Duan C et al., 2016).

Rutile (TiO_2), one of common accessory minerals, is widely hosted within various rocks (Xiao YL et al., 2011), which is also an important host for high field strength elements (Nb, Ta, Zr) (Meinhold G, 2010). In general, trace element compositions of rutile can be used to provide insights into protolith (Xiao YL et al., 2011). For example, the Fe contents in rutile can be applied to calculate oxygen fugacity during crystallization (Sobolev NV and Yefimova ES, 2000;

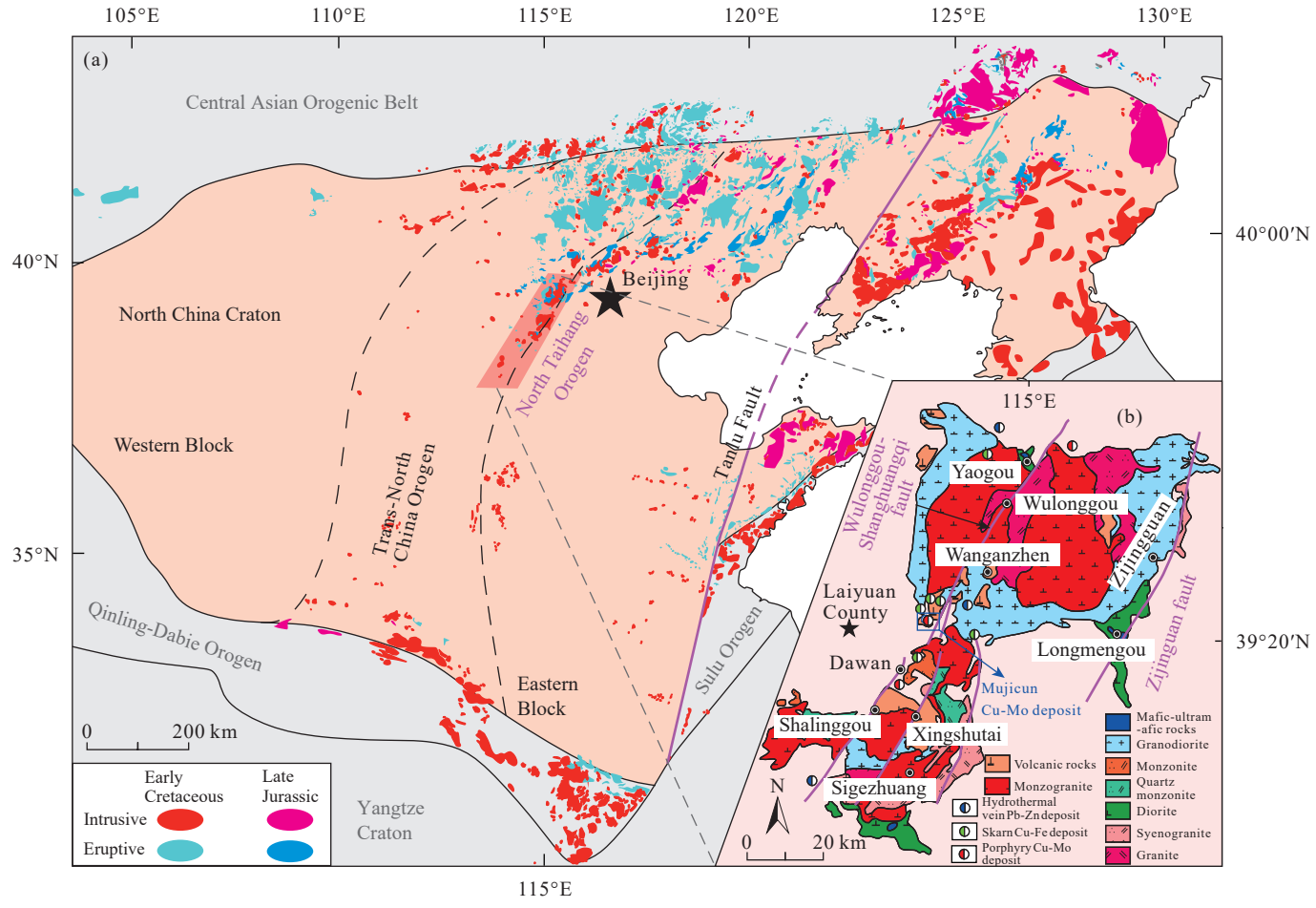

Fig. 1. Tectonic map of the North China Craton with the spatial-temporal variation of the Late Jurassic to Early Cretaceous magmatic rocks (a, after Zhao G et al., 2005; Zhang SH et al., 2014) and geological map of the Laiyuan complex with the distribution of major lithologic units, ore deposits and faults (b, after Xue F et al., 2021).

Meinhold G, 2010), the Zr contents in rutile can be employed as the geothermometer with temperature range of 400–1100°C (Zack TV et al., 2004a; Ferry JM and Waston EB, 2007) and used to constrain the *P-T-t* conditions during metamorphism (Zheng YF et al., 2011), the Nb and Cr contents in rutile could be devoted to trace rutile source from metacumulates, meta-mafic and metapelitic rocks (Zack TV et al., 2004b). Usually, the rutile from cratonic mantle has higher Cr contents than 1.7%, whereas those from crust and non-cratonic mantle are lower than 1.7% (Malkovets VG et al., 2016). The Mg and Al contents in mantle-derived rutile are higher than those from crust-derived rutile (Smythe D et al., 2008). The Nb/Ta ratios in rutile can also be applied to reveal the formation evolution of crust and to trace subduction processes (Tang M et al., 2019; Xiao Y et al., 2006). Thus, it could be drawn the conclusion that rutile trace elements can be selected to trace magma source and magma evolution as well as to guide mineral exploration of diamond and related deposits (Rabbia OM et al., 2009; Schmidt MW et al., 2004; Porter JK et al., 2020). Due to similar ionic radius and valence states of U^{4+} and Ti^{4+}, the U with respect to Pb preferentially enters into lattice, resulting in the U contents in rutile enriched up to 200×10^{-6} (Xiao YL et al., 2011). Also, rutile is extremely resistant to isotopic resetting, it thus can be used for U-Pb dating, with closure temperature of 370–600°C (Mezger K et al., 1989; Vry JK and Baker JA, 2006). As a result, rutile U-Pb dating has been widely used to determine the cooling ages of metamorphic and magmatic rocks (Bibikova E et al., 2001; Li Q et al., 2003; Hou Z et al., 2020) and the ore-forming ages of gold, copper and other deposits (Pi QH et al., 2017; Schirra M and Laurent O, 2021; Xiao X et al., 2021; Cluzel D et al., 2022).

In this study, this paper carried out systematic petrological and *in situ* LA-ICP-MS U-Pb dating and trace element composition studies of rutile from ore-hosting diorite porphyry in the Mujicun Cu-Mo deposit, North China Craton (Fig. 1). Combined with published geochronological, geochemical and isotopic studies from the Mujicun Cu-Mo deposit, the major objectives of this paper are to clarify the timing and timescales of Cu-Mo mineralization, and to reveal magma source, ore genesis and tectonic evolution of the Mujicun Cu-Mo deposit. Additionally, this study would also provide insights into intra-continental porphyry Cu-Mo mineralization.

2. Geological setting

2.1. Regional geology

The NCC (Fig. 1a) is located between the Central Asian Orogenic Belt and Qinling-Dabie Orogenic Belt (Xiao W et al., 2012; Gao YF et al., 2013). Tectonically, the NCC is divided into the Western Block, the Eastern Block and the intervening Trans-North China Orogen (Zhao G et al., 2005; Zhao G and Zhai M, 2013), which comprises Precambrian metamorphic basement, Mesoproterozoic (1.8 Ga) to Cenozoic sedimentary cover sequences, and Mesozoic intrusions (Zhai MG and Santosh M, 2011; Yang F et al., 2021a). The Mesozoic magmatic rocks have been widely correlated with the lithospheric thinning and craton destruction of the NCC (Wu FY et al., 2011; Zhu RX et al., 2012a, 2012b; Yang F et al., 2018a, 2018b, 2020a), which are divided into the Early Triassic, the Middle-Late Triassic, the Early Jurassic-earliest Middle Jurassic, the Middle-Late Jurassic, the Early Cretaceous, and the Late Cretaceous periods (Zhang SH et al., 2014). The Early Triassic intrusive rocks are readily identified throughout the east-west-trending Yinshan and Yanshan belts along the northern margin of the NCC and in the southern Yanbian–Liaobei area of the northeastern NCC (Wu FY et al., 2007; Zhang SH et al., 2014). The Middle–Late Triassic magmatic rocks are also mainly exposed in the Yinshan and Yanshan belts of the northern NCC and the Liaodong as well as the southern Yanbian–Liaobei area of the eastern NCC (Wu FY et al., 2005, 2007; Yang J and Wu F, 2009; Hou ZQ et al., 2015). The minor Early Jurassic–earliest Middle Jurassic intrusive rocks are mostly outcropped in the Yanshan belt and the Beiiing West Hills of the northern NCC (Wu FY et al., 2011; Liu J et al., 2012; Lan TG et al., 2012; Zhang SH et al., 2014). The Middle–Late Jurassic intrusive rocks are largely confined to the Yanshan Belt of the northern NCC, the Liaodong and Jiaodong Peninsula of the eastern NCC, and the southern Yanbian-Liaobei area of northeastern NCC (Fig. 1a; Wu FY et al., 2011). The Early Cretaceous magmatic rocks intruded throughout the eastern and central NCC (Fig. 1a), and the Late Cretaceous volcanic rocks are exposed in the eastern NCC (Yang F et al., 2018a; Zhang SH et al., 2014).

The North Taihang Orogen, located in the middle-eastern margin of the Trans-North China Orogen (Fig. 1a), hosts numerous Jurassic to Cretaceous magmatic rocks associated with Cu-Mo-Fe polymetallic mineralization (Fig. 1b; Dong GC et al., 2013; Gao YF et al., 2013; Xue F et al., 2019, 2021; Yang F et al., 2019). The strata outcropped in this orogen consist mainly of the Archean high-graded metamorphic series, the tonalite-trondhjemite-granodiorite (TTG) series, and the unconformably overlying Mesoproterozoic to Mesozoic volcanic-sedimentary rocks (Qu K et al., 2014; Dong GC et al., 2013). The Mesozoic intrusions in this orogen mostly occur as batholiths and stocks, including Sigezhuang, Mapeng, Ciwawu and Wanganzhen intrusions (Wang Y and Li H, 2008; Zhang HD et al., 2016), which intruded along the NNE-trending faults. The Wanganzhen complex (Fig. 1b), one of the biggest intrusions in the North Taihang Orogen, mainly comprise granodiorite, monzogranite and porphyritic granite, as well as some volcanic rocks along its northwestern and southwestern margins (Gao YF et al., 2011, 2013; Xue F et al., 2021). A few diorite, syenogranite and hornblendite are also found in the east of this complex (Fig. 1b). Based on the lithology and zircon U-Pb ages, the Wanganzhen complex is divided into the early phase (223–187 Ma) of intermediate-mafic magmatic rocks, the middle phase (146–138 Ma) of intermediate-felsic magmatic rocks, along with the late phase (about 126 Ma) of alkaline-

rich intermediate-felsic magmatic rocks (Cai JH et al., 2003; Zhang HD et al., 2016). The faults developed in this orogen mainly include the NE-trending Wulonggou–Shanghuangqi and Zijingguan faults as well as their NE-striking branches (Fig. 1b; Dong GC et al., 2013; Gao YF et al., 2013). In addition, three different genetic types of metallic deposits also developed along the margin of the Wanganzhen complex (Fig. 1b): porphyry Cu-Mo deposits in its northern and southwestern margins, skarn Fe-Cu deposits restricted to northern margin and central domains, and hydrothermal vein Pb-Zn deposits in its northern and southwestern margins (Gao YF et al., 2013; Qu K et al., 2014; Shen ZC et al., 2015; Chen C et al., 2015).

2.2. Deposit geology

The Mujicun porphyry Cu-Mo deposit is located in the Mujicun village and is about 20 km distance at the northeast of the Laiyuan County (Fig. 1b). Tectonically, it lies between the southwestern margin of Wanganzhen complex and the regional Wulonggou fault (Fig. 1b). The strata exposed in this deposit mainly include the Proterozoic dolomite and sandstone, the Cambrian-Ordovician limestone, the Jurassic volcanic breccia, and the overlying Quaternary sediments (Gao YF et al., 2011). The NNE-trending Wulonggou-Shanghuangqi fault and its branches are the major ore-controlling structure (Fig. 1b). The magmatic rocks of this deposit consist mainly of andesite, intermediate-basic, lamprophyre and albitophyre dikes and diorite porphyry (Hou T et al., 2015; Shen ZC et al., 2015). The andesite is distributed in the northeastern margin of this deposit, whereas the dikes mostly intruded along fault zones (Fig. 2). The diorite porphyry as stock usually occurs at the central domain of the Mujicun deposit. The diorite porphyry stock shows a length of about 1 km and a width of about 0.4 km, with an area of about 1.5 km^2 (Fig. 2). Most of diorite porphyry at earth surface was altered by propylitization, whereas those discovered in the center of concealed diorite porphyry stocks underwent beresitization (Qu K et al., 2014).

The orebodies are all concealed and hosted in diorite porphyry as well as skarn at contact zones between diorite porphyry and wall rocks, with average Cu grades of 0.26%–0.49% and Mo grades of 0.04%–0.14% (Chen C et al., 2013; Shen ZC et al., 2015). The orebodies occur as irregular lenticles, characterized by the NNE-trending strike, SE-trending inclination, with the dips of 52°–80° (Chen C et al., 2015). These orebodies are divided into two ore belts in vertical direction (Fig. 3). The upper ore belt is dominated by porphyry Cu-Mo ores and minor skarn Cu-Fe ores that are hosted at the depth of 200–850 m below the surface, with a length of about 900 m from south to north, a width of

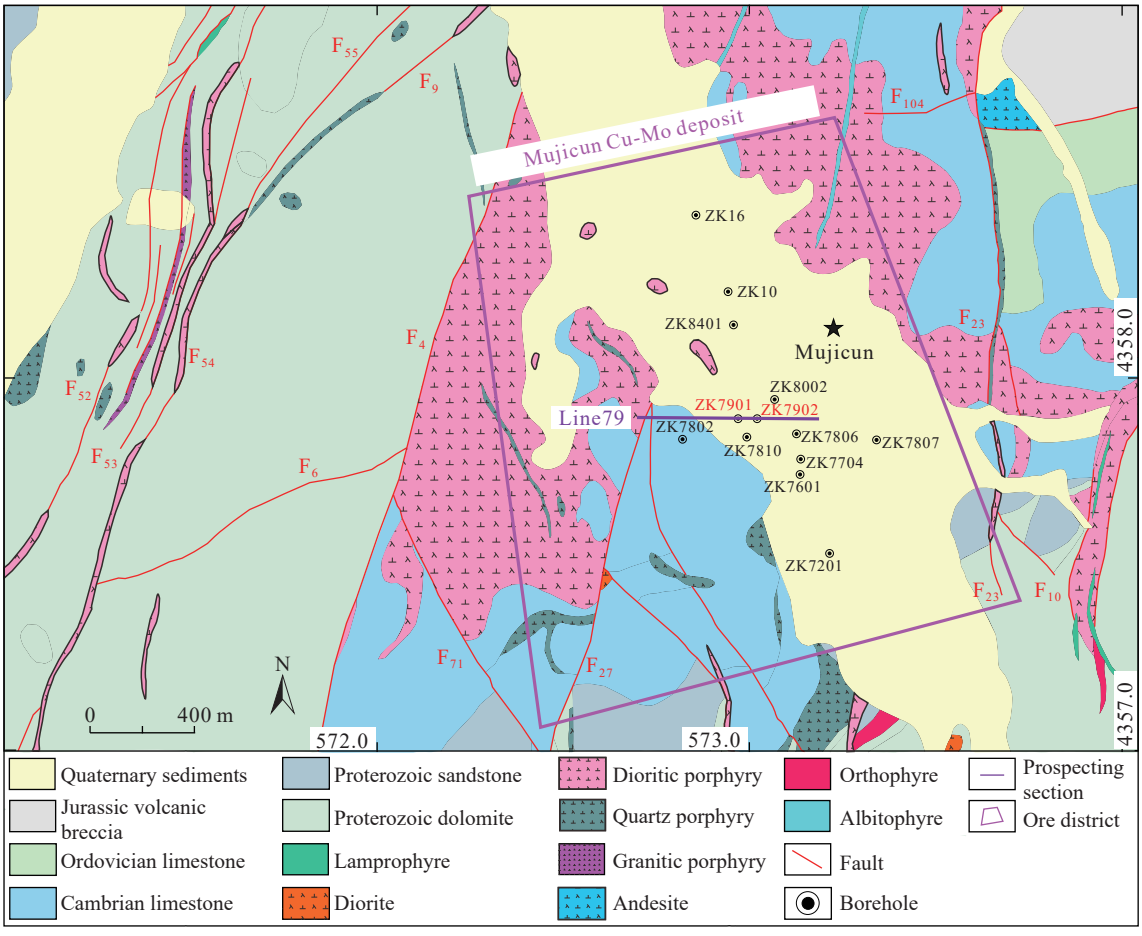

Fig. 2. Geological map of the Mujicun Cu-Mo deposit and adjacent regions showing major lithologic units and faults as well as the locations of boreholes (after Dong GC et al., 2013).

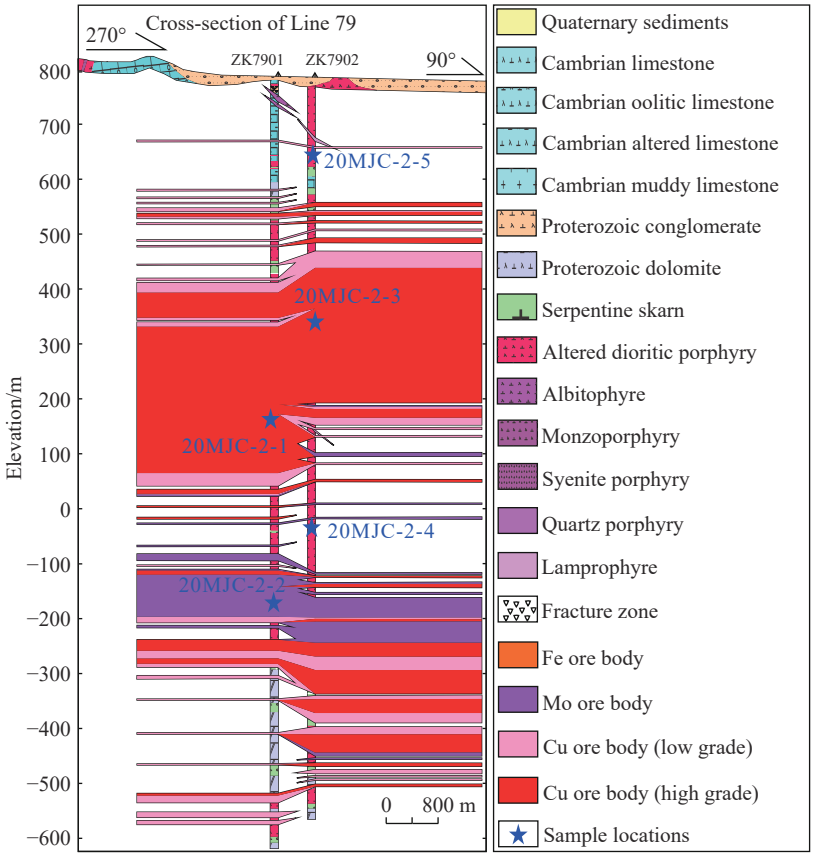

Fig. 3. Exploration cross-section of Line 79 in the Mujicun Cu-Mo deposit showing the spatial distribution of lithologic units, orebodies and sampling locations.

180–790 m from east to west, and a thickness of 18–344 m (mean: 217 m). The lower ore belt is mainly represented by skarn Cu (Mo) ores and partial porphyry Cu or Cu-Mo ores which are discovered at the depth of 800–1300 m below the surface. The lower ore belt has a length of about 400 m, a width of 460–700 m, and a thickness of 67–393 m (mean: 248 m) (Chen C et al., 2013). The ores in this deposit mainly contain Cu, Cu-Mo and Mo ores (Fig. 3) and are divided into porphyry and skarn ores, which mostly display fine-grained, disseminated and veined texture (Chen C et al., 2015). The metal minerals of these ores mainly include chalcopyrite, pyrite and molybdenite, whereas the gangue minerals are dominated by K-feldspar, plagioclase and quartz (Gao YF et al., 2013; Chen C et al., 2015). The alteration types are mainly composed of silicification, K-feldspathization, sericitization and propylitization from the center of porphyry to its periphery (Ma G, 1997). The K-feldspathization is closely correlated with the porphyry Cu-Mo mineralization (Gao YF et al., 2013). The metallogenic stages of the Mujicun deposit are summarized as: (1) skarn Cu-bearing magnetite, (2) porphyry Cu-Mo, (3) skarn Cu-Fe, and (4) hydrothermal Pb-Zn mineralization from early to late stages (Ma G, 1997).

3. Sampling and petrography

A total of five representative samples were taken from boreholes ZK7901 and ZK7902 in this study, and the detailed locations are shown in Figures 2 and 3. Sample 20MJC-2-1 is a Cu-rich diorite porphyry and collected from borehole ZK7901 at a depth of 644 m. Sample 20MJC-2-2 is a Mo-rich diorite porphyry and taken from borehole ZK7901 at a depth of 963 m (Fig. 3). Samples 20MJC-2-4 and 20MJC-2-5 are all ore-barren diorite porphyry, which were sampled from borehole ZK7902 at depths of 822 m and 159 m, respectively. Sample 20MJC-2-3 is also a Cu-rich diorite porphyry and taken from borehole ZK7902 at a depth of 461 m (Fig. 3). All five diorite porphyry samples are gray to black colored and show porphyritic texture and underwent slight alteration of silicification (Fig. 4). The diorite porphyry mainly includes plagioclase phenocrysts (Fig. 4i) and is interspersed with several quartz veins carrying Cu-Mo mineralization inside (Fig. 4d–f).

Under microscopes, all samples display typical porphyritic texture and consist mainly of subhedral-euhedral biotite (0.2–0.5 mm), polysynthetic plagioclase (0.4–0.7 mm), and slightly corroded hornblende phenocrysts together with matrix including fine-grained felsic minerals and accessary minerals (zircon, rutile, apatite) (Fig. 5a–f). Among these, the rutile mostly grew within the interstices of quartz and feldspar (Fig. 5e). Moreover, several quartz veins also developed in diorite porphyry (Fig. 5a–e). Sample 20MJC-2-5 underwent weak alteration of albite and zoisitization (Fig. 5f). The metal minerals of diorite porphyry mainly contain chalcopyrite, pyrite and molybdenite (Fig. 5g–i). The chalcopyrite is mostly disseminated and intergrew at gaps of felsic minerals (Fig. 5g, i), which often coexisted with pyrite and molybdenite in

Fig. 4. Representative field photographs of diorite porphyry from boreholes in the Mujicun Cu-Mo deposit.

quartz veins (Fig. 5h). The pyrite and molybdenite are sporadic and usually occur at mineral gaps or within quartz veins (Fig. 5g–i).

4. Analytical methods

Rutile grains were separated in the Yu'neng Geological and Mineral Separation Survey Centre, Langfang, Hebei, China, using standard mineral separation procedures. Transmitted, reflected light, cathodoluminescence (CL) and back-scattered electron (BSE) images were captured to investigate the internal structures of rutile and to identify target sites for rutile geochemical and U-Pb isotopic analysis. Rutile U-Pb dating and geochemical analysis was simultaneously performed at the Tianjin Center, China Geological Survey, using a Neptune multi-collector inductively coupled plasma mass spectrometer equipped with a New Wave 193 nm laser sampler. The ablation was set as a spot size of 51 μm, with a frequency of 7 Hz and a fluence of 3 J/cm^2. Rutile RMJG (Zhang L et al., 2020) and Glass SRM610 (Pearce NJ et al., 1997) were selected as external standards to conduct fractionation correction of rutile U-Pb isotope and trace element data, following the detailed methods noted by Zhou HY et al. (2013). During this analysis, one SRM610 and two RMJG standards as well as six unknown rutile grains were grouped as each analytical session. Each analysis on the rutile began with a 15 seconds blank gas measurement, then followed by a further 50 seconds of analysis time when the laser was switched on. Data reduction was performed using the ICPMSDataCal software to finish the selection of sample and blank signal, the correction of instrument drift and mass bias, and the calculation of element contents, isotopic ratios and age data. Rutile RMJG standard was also selected to correct rutile U-Pb age. Glass SRM610 as an external standard was employed to correct trace element concentrations, whereas ^{49}Ti was used as an internal standard to correct trace element data. The IsoplotR (Vermeesch P, 2018) and Origin (Edwards PM, 2002) software were chosen to process age and trace element data with one sigma uncertainty.

5. Results

5.1. Rutile morphology and U-Pb geochronology

A total of one hundred and fifteen rutile grains from samples 20MJC-2-1, 20MJC-2-2 and 20MJC-2-3 were selected for U-Pb dating, and the analytical data are given in Table DR1.

These rutile grains are transparent to translucent and brown to colorless, and show prismatic to sub-round in shape, with size varying between 50 μm and 150 μm and length to width ratios from 3∶1 to 1∶1 (Fig. 6a–c). Under CL and BSE images (Fig. 6), most of rutile grains show homogeneous gray to dark structureless and unzoned texture, and a few grains have weak patchy zoning texture. Furthermore, several mineral or fluid inclusions also widely developed in the interior of individual rutile under BSE images (Fig. 6b–c).

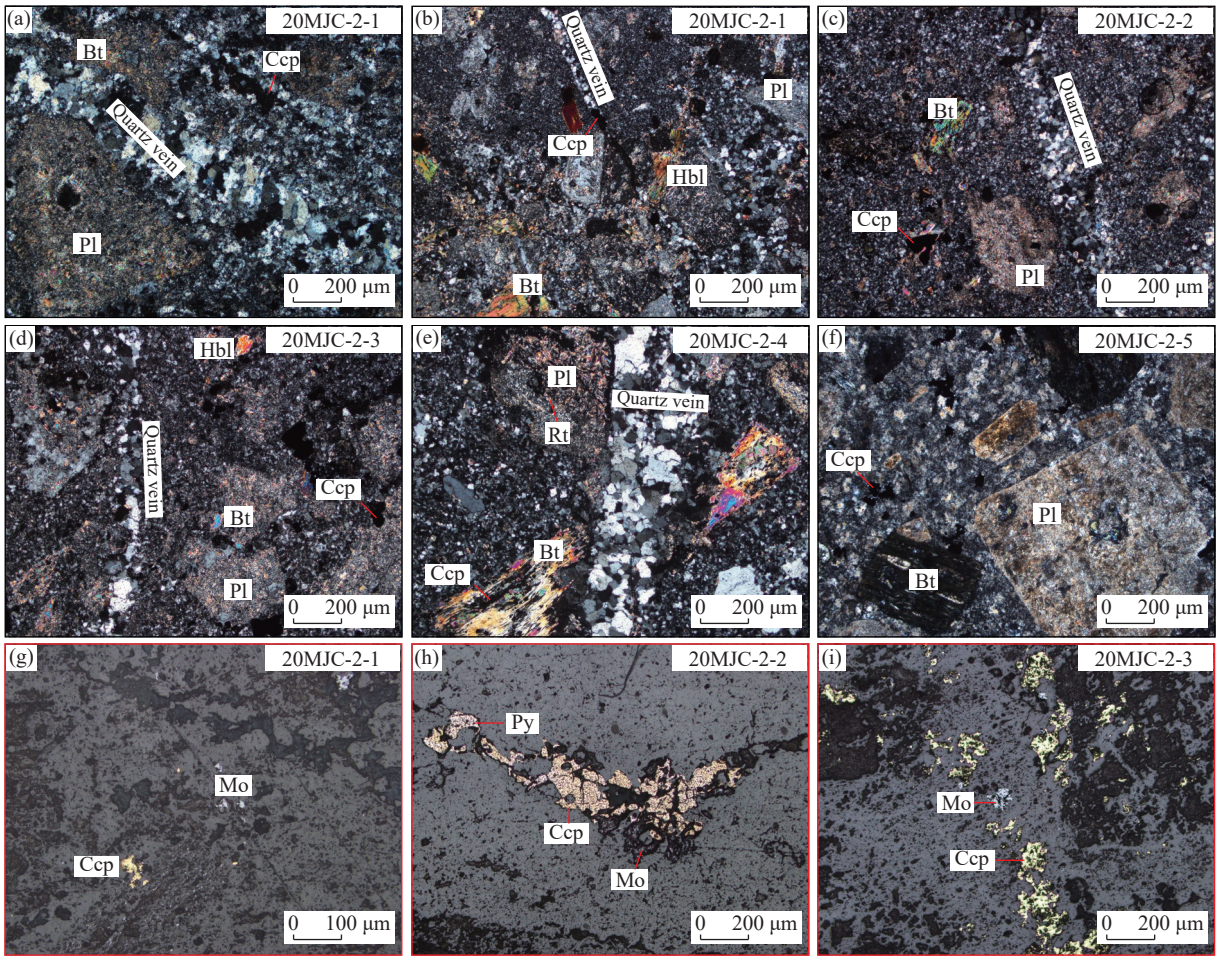

Fig. 5. Photomicrographs of diorite porphyry from boreholes in the Mujicun Cu-Mo deposit. a–f: cross-polarized light; g–i: reflected light. Mineral abbreviations: Pl–plagioclase; Bt–biotite; Hbl–hornblende; Rt–rutile; Ccp–chalcopyrite; Mo–molybdenite; Py–pyrite.

Thirty-eight rutile grains from sample 20MJC-2-1 yield a lower intercept age of 139.3 ± 33 Ma (MSWD = 0.58) (Fig. 6d), with Th and U contents and Th/U ratios of 0.00×10^{-6}–3.79×10^{-6}, 0.64×10^{-6}–16.35×10^{-6}, and 0.01–0.71, respectively. Thirty-eight rutile grains from sample 20MJC-2-2 yield a lower intercept age of 138.6 ± 2.3 Ma (MSWD = 1.40) (Fig. 6e) and have Th contents of 0.00×10^{-6}–14.15×10^{-6}, U contents of 0.44×10^{-6}–56.26×10^{-6} and Th/U ratios of 0.00–0.73. Thirty-nine rutile grains from sample 20MJC-2-3 display Th contents mostly in the range of 0.00×10^{-6}–1.69×10^{-6}, U contents of 0.66×10^{-6}–21.19×10^{-6} and Th/U ratios of 0.00–0.59, which yield a lower intercept age of 138.4 ± 5.1 Ma (MSWD = 0.39) (Fig. 6f).

5.2. Rutile trace element geochemistry

One hundred and fifteen rutile grains used for U-Pb dating were also selected for geochemical analysis, and the obtained geochemical data are shown in Table DR2. During this analysis, only the major element of ZrO_2 is determined. The studied rutile grains mostly show ZrO_2 contents in the range of 0.01%–0.16%, with only two rutile grains displaying abnormally high ZrO_2 values of 0.42% and 24.84%. Other geochemical data include trace (Mg, Al, V, Cr, Fe, Co, Ni, Cu, Zn, As, Y, Nb, Mo, Ag, Sn, Sb, Hf, Ta, W) and rare earth (REE: La-Lu) elements. Note that the trace elements of Co, Ni, Zn, Y, Ag, Sn and Hf in rutile are not employed for further interpretation in following texts, and these data are only listed in the Table DR2.

Except for a few abnormal values, the Mg contents in samples 20MJC-2-1, 20MJC-2-2 and 20MJC-2-3 mostly vary from 122.60×10^{-6} to 374.91×10^{-6}. The Al contents in samples 20MJC-2-1 and 20MJC-2-2 show similar variation range of 5.39×10^{-6}–97.15×10^{-6}, whereas sample 20MJC-2-3 has two distinct populations of Al contents varying from 10.83×10^{-6} to 327.72×10^{-6} and 1008.05×10^{-6} to 1473.86×10^{-6}. The V contents in sample 20MJC-2-1 vary from 990.13×10^{-6} to 2192.43×10^{-6}, with a mean value of 2486.66×10^{-6}. Whereas samples 20MJC-2-2 (range: 1510.25×10^{-6}–5270.75×10^{-6}; mean: 3344.47×10^{-6}) and 20MJC-2-3 (range: 1032.19×10^{-6}–4529.23×10^{-6}; mean: 3431.93×10^{-6}) have similar V contents. The Cr contents in sample 20MJC-2-1 (range: 84.18×10^{-6}–8596.33×10^{-6}; mean: 2632.98×10^{-6}) are much higher than samples 20MJC-2-2 (range: 153.75×10^{-6}–2940.34×10^{-6}; mean: 734.77×10^{-6}) and 20MJC-2-3 (range: 298.45×10^{-6}–3162.75×10^{-6}; mean: 885.44×10^{-6}). The Fe contents in sample 20MJC-2-1 (range: 457.09×10^{-6}–5253.78×10^{-6}; mean: 1695.28×10^{-6}) are lower than samples 20MJC-2-2 (range: 1017.16×10^{-6}–4433.45×10^{-6}; mean: 2130.94×10^{-6})

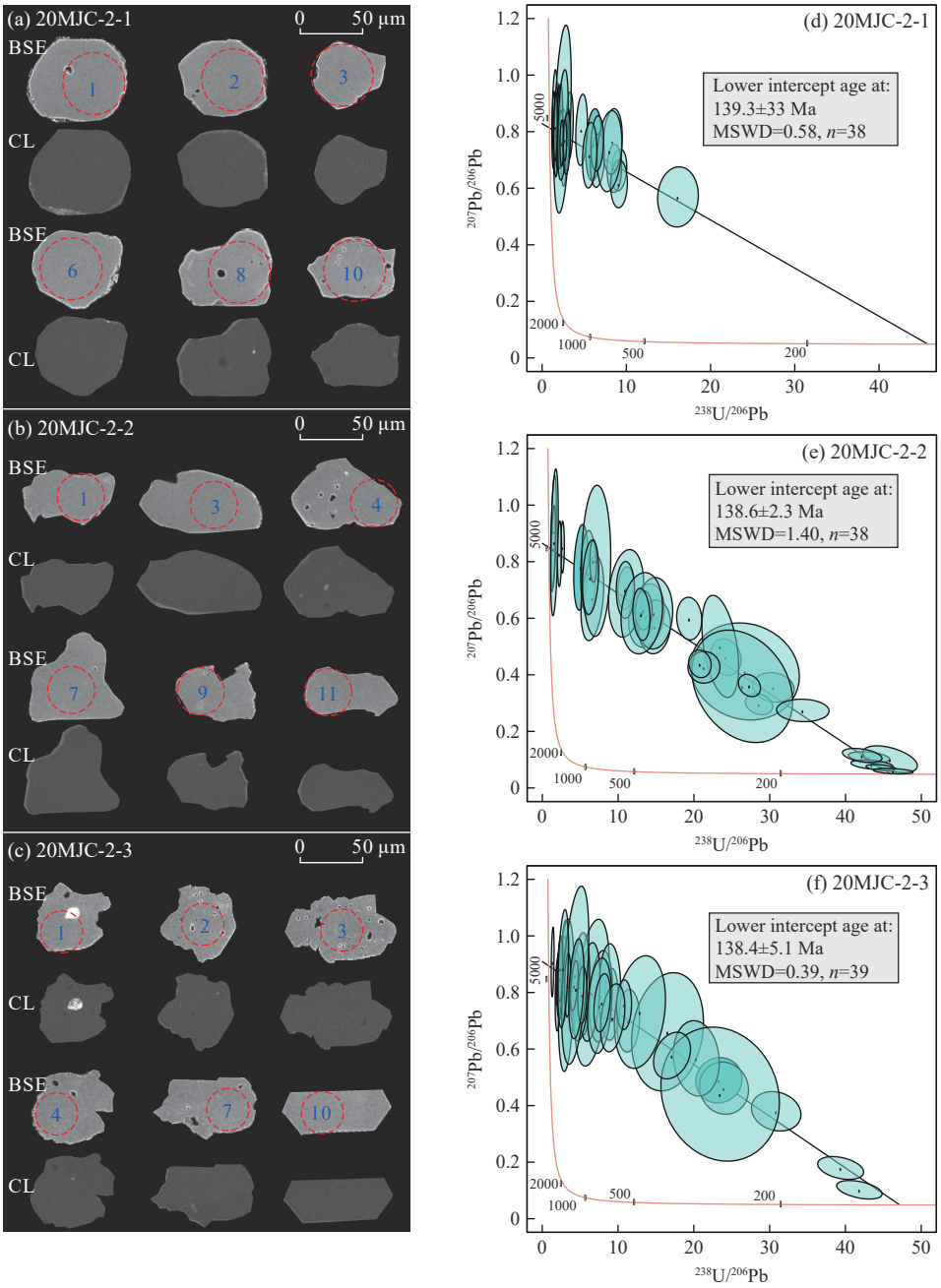

Fig. 6. Representative rutile CL and BSE images marked with analytical positions and spot numbers (a–c) and rutile U-Pb Terra-Wasserburg concordia plots (d–f) of diorite porphyry taken from boreholes in the Mujicun Cu-Mo deposit.

and 20MJC-2-3 (range: 590.56×10^{-6}–5665.32×10^{-6}; mean: 2463.67×10^{-6}). The Cu contents in sample 20MJC-2-1 range from 1.11×10^{-6} to 5.81×10^{-6} (mean: 1.97×10^{-6}) and are relatively lower than samples 20MJC-2-2 (range: 1.16×10^{-6}–20.31×10^{-6}; mean: 4.48×10^{-6}) and 20MJC-2-3 (range: 1.03×10^{-6}–130.02×10^{-6}; mean: 15.25×10^{-6}). The As contents in all analyzed samples have similar variation range of 0.00×10^{-6}–2.81×10^{-6} and mean values of 0.18×10^{-6}–0.37×10^{-6}. The Nb contents in all analyzed samples mostly vary from 102.78×10^{-6} to 4240.88×10^{-6}, with mean values of 1279.02×10^{-6}–1524.92×10^{-6}. The Mo contents in samples 20MJC-2-1 and 20MJC-2-3 show similar variation range of 5.41×10^{-6}–83.76×10^{-6} and mean values of 35.45×10^{-6}–39.06×10^{-6}, which are relatively lower than sample 20MJC-2-2 (range: 6.39×10^{-6}–116.88×10^{-6}; mean: 55.13×10^{-6}). The Sb contents in all analyzed samples have similar variation range from 0.00×10^{-6}–1.39×10^{-6} and mean values of 0.12×10^{-6}–0.17×10^{-6}. The Ta contents in all analyzed samples range from 2.76×10^{-6} to 130.71×10^{-6} and have mean values of 44.26×10^{-6}–45.43×10^{-6}. The W contents collectively vary from 120.89×10^{-6} to 5805.26×10^{-6}, with the highest values in sample 20MJC-2-3 (range: 287.24×10^{-6}–4696.60×10^{-6}; mean: 1094.99×10^{-6}) and the lowest values in sample 20MJC-2-1 (range: 120.89×10^{-6}–949.02×10^{-6}; mean: 417.84×10^{-6}).

The total REE (ΣREE) concentrations of 115 rutile grains from samples 20MJC-2-1, 20MJC-2-2 and 20MJC-2-3 show wide variation in the range of 0.34×10^{-6}–665.42×10^{-6}, with

an abnormally high value of 3684.13×10^{-6} in sample 20MJC-2-3. Among these, sample 20MJC-2-3 have relatively lower ΣREE concentrations of 0.34×10^{-6} –10.68×10^{-6} and a lower mean value of 3.53×10^{-6}, other samples show higher corresponding values, such as 20MJC-2-1 (range: 2.30×10^{-6}–665.42×10^{-6}; mean: 91.85×10^{-6}) and 20MJC-2-2 (range: 0.41×10^{-6}–551.82×10^{-6}; mean: 41.19×10^{-6}). The light REE (La-Eu) (ΣLREE) of samples 20MJC-2-1, 20MJC-2-2 and 20MJC-2-3 are mostly in the range of 1.61×10^{-6}–640.56×10^{-6} (mean: 81.79×10^{-6}), 0.00×10^{-6}–465.34×10^{-6} (mean: 29.48×10^{-6}) and 0.11×10^{-6}–9.03×10^{-6} (mean: 2.60×10^{-6}), whereas the heavy REE (Gd-Lu) (ΣHREE) of these samples ranges from 0.39×10^{-6}–109.12×10^{-6} (mean: 10.06×10^{-6}), 0.07×10^{-6}–205.11×10^{-6} (mean: 11.71×10^{-6}) and 0.09×10^{-6}–6.77×10^{-6} (mean: 0.93×10^{-6}). The ΣLREE/ΣHREE ratios of rutile display wide variation range from 1.33×10^{-6}–33.34×10^{-6} (20MJC-2-1), 0.00×10^{-6}–31.51×10^{-6} (20MJC-2-2) and 0.05×10^{-6}–28.93×10^{-6} (20MJC-2-3). In the chondrite-normalized REE patterns (Fig. 7a–c), samples 20MJC-2-1, 20MJC-2-2 and 20MJC-2-3 display flat-like REE patterns, characterized by relatively enrichment in LREEs and depletion of HREEs. The $(Eu/Eu^*)_N$ values of these samples are mostly lower than 1.00, with variation range of 0.00–0.97 (n = 26) for sample 20MJC-2-1, 0.00–0.88 (n = 22) for sample 20MJC-2-2, and 0.00–0.87 (n = 20) for sample 20MJC-2-3, suggesting weak to moderate Eu negative anomalies. In addition, these samples also show a few $(Eu/Eu^*)_N$ values varying from 1.00 to 4.60 (>1.00), indicating Eu positive anomalies. The rutile $(Ce/Ce^*)_N$ values in all analyzed samples range from 0.00 to 41.29 (n = 115), but most of these (n = 74) are lower than 1.00.

6. Discussion

6.1. Genetic types of rutile from the Mujicun Cu-Mo deposit

Previous studies indicated that the genetic types of rutile could be divided into magmatic, hydrothermal, metamorphic and detrital origin (Cai JH et al., 2008; Scott KM and Radford NW, 2007). Given that the studied rutile grains were crystalized in diorite porphyry and the Fe contents (457.09×10^{-6}–5665.32×10^{-6}) in these rutile are lower than metamorphic rutile (0.13%; Zack TV et al., 2004b), this study thus excludes the metamorphic and detrital origin. Accordingly, the genetic types of the studied rutile fall into magmatic or hydrothermal origin. Cai JH et al. (2008) summarized that magmatic rutile is usually generated by the crystallization of high Si, low Fe and Ti magma produced through initial magmatic differentiation, or high Ti and Fe magma that was produced by carbonate magma captured high Ti and Fe-rich components. Hydrothermal rutile is often formed by the high Ti hydrothermal fluids which migrated and emplaced along structural fractures under oxidizing conditions, or the releasing Ti from high titanium rocks that host abundant ilmenite, biotite, and hornblende during hydrothermal alteration (Cai JH et al., 2008).

In the Mujicun Cu-Mo deposit, previous studies suggested

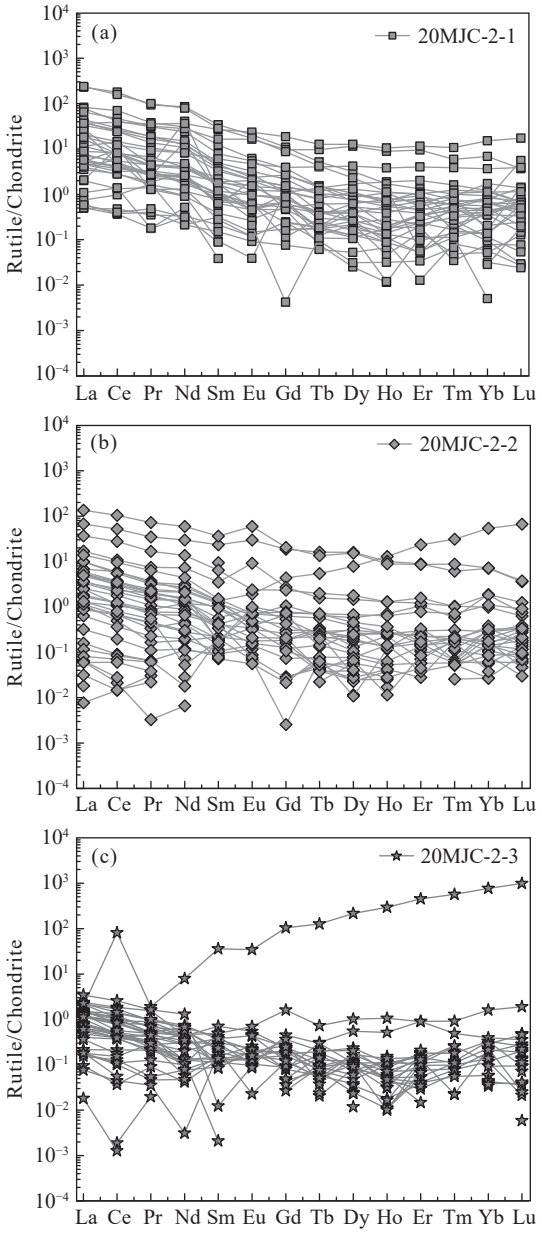

Fig. 7. Chondrite-normalized rutile REE patterns of diorite porphyry taken from boreholes in the Mujicun Cu-Mo deposit. Chondrite-normalized values are from Sun SS and McDonough WF (1989).

that their ore-hosting diorite porphyry belong to high-K calc-alkaline I-type granitoids and underwent partial melting of ancient lower crust (Dong GC et al., 2013; Qu K et al., 2014) or enriched mantle (Gao YF et al., 2013; Shen ZC et al., 2015; Duan C et al., 2016) as well as subsequent fractional crystallization of amphibole and accessory minerals of Fe-Ti oxides, titanite, zircon and apatite (Gao YF et al., 2013), but it remains difficult to distinguish the genetic types of rutile between the magmatic and hydrothermal origin. Geochemically, hydrothermal rutile from related metallic deposits is identified to have high abundances of W, V, Sr, Cu, Sn, and Sb, distinguished from those crystalized in magmatic and metamorphic rocks (Clark JR and Williams-Jones AE, 2004; Scott KM, 2005). More specifically, hydrothermal rutile shows high W (up to order of magnitude

of 10^{-2}) and V (up to order of magnitude of 10^{-2}) as well as low Zr (order of magnitude of 10^{-6}) contents (Clark JR and Williams-Jones AE, 2004). In this study, the rutile grains in the Mujicun deposit have low W (120×10^{-6}–5806×10^{-6}) and V (990×10^{-6}–5271×10^{-6}) along with high ZrO_2 (mostly 0.01%–0.16%) contents (Table DR2), which are uncommon with hydrothermal rutile. Coupled with the studied rutile grains crystalized at the interstices of quartz and feldspar in diorite porphyry (Fig. 5e), this study therefore proposes that the genetic type of the studied rutile from the Mujicun Cu-Mo deposit is of magmatic origin.

6.2. Temporal constraints on the Mujicun Cu-Mo deposit

In general, through determining rutile parent/daughter isotopic ratios and known decay constants, the rutile U-Pb dating could be used to calculate the timing when rutile cooled below its closure temperature (Meinhold G, 2010). The closure temperature of rutile U-Pb dating system was usually measured at around 600°C (Cherniak DJ, 2000; Vry JK and Baker JA, 2006) or 370–500°C (Mezger K et al., 1989). Based on the Zr-in-rutile thermometry (Zack TV et al., 2004a; Watson EB et al., 2006), the formation temperature of rutiles from the Mujicun deposit is determined mostly in the range of 574–925°C, with an average value of 701°C (Table DR2). Accordingly, the U-Pb ages (139.3–138.4 Ma; Fig. 6) of magmatic rutile can be employed to constrain the cooling ages of diorite porphyry in the Mujicun deposit. In addition, the fluid inclusion data of quartz, calcite and fluorite in the Mujicun Cu-Mo deposit constrained its ore-forming temperature varying from 103–472°C (Chen C et al., 2013), which overlapped with the lower-bound of rutile U-Pb closure temperature. Thus, the rutile U-Pb dating is sensitive to the ore-forming geochronological signals of the Mujicun Cu-Mo deposit, and the ore-forming age of the Mujicun deposit could be constrained at 139.3–138.4 Ma (Fig. 6), which is also evidenced by previous studies related to the rutile U-Pb dating in other porphyry Cu deposits (Schirra M and Laurent O, 2021; Xiao X et al., 2021). Accordingly, the dating results also support a possible temporal correlation between the formation of the Mujicun Cu-Mo mineralization and the later large-scale granitic magmatism during 138–126 Ma in the Taihang Orogen (Chen B et al., 2005).

Although the epidote skarn at contact zones between diorite porphyry and wall rocks in the Mujicun Cu-Mo deposit yielded two zircon U-Pb mean ages of 146.2 Ma and 139.9 Ma, Dong GC et al. (2013) interpreted 146.2 Ma as the inherited zircon age from diorite porphyry and 139.9 Ma as the timing of skarn formation. In contrast, the newly determined rutile U-Pb ages of the diorite porphyry (139.3–138.4 Ma) are consistent or slightly postdate with the formation age of diorite porphyry (zircon U-Pb ages: 144.1–141.7 Ma), molybdenite (Re-Os ages: 144.8–140.0 Ma) and skarn (zircon U-Pb ages: 139.9 Ma) in the Mujicun Cu-Mo deposit (Fig. 8a). Published zircon $^{206}Pb/^{238}U$ spot ages (range: 149.0–129.0 Ma; peak value: 143.7 Ma) of diorite porphyry highly overlap with the molybdenite Re-Os model ages (range: 145.5–138.5 Ma; peak value: 143.2 Ma) in the Mujicun Cu-Mo deposit (Figs. 8b-c). Combined with the closure temperatures of zircon U-Pb (>900 °C; Cherniak DJ and Watson EB, 2001) and of molybdenite Re-Os dating (about 500°C; Suzuki K et al., 1996), this study further suggests that the diorite porphyry underwent rapid post magmatic cooling below about 500°C in response to host-rock thermal equilibration as well as shallow emplacement.

6.3. Source and ore genesis of the Mujicun Cu-Mo deposit

Smythe D et al. (2008) proposed that Mg and Al contents in rutile could be used to trace magma nature derived from crust and mantle compositions. In this study, most of rutile geochemical data plot in the field of crust-derived rutile, with a few plots which occur in the mantle-derived rutile field (Fig. 9a), suggesting that magma is mainly sourced from ancient crust with minor input of mantle components. In addition, the Cr contents in the studied rutile (84.18×10^{-6}–8596.33×10^{-6}; Table DR2) are far lower than 1.7%, which also suggest crustal source for diorite porphyry (Malkovets VG et al., 2016). The crust-mantle mixing magma source features are also attested by whole-rock Sr-Nd-Pb ($\varepsilon_{Nd}(t)$ = −13.1–−16.7) (Gao YF et al., 2013; Qu K et al., 2014; Hou ZQ et al., 2015) and zircon Lu-Hf isotopes ($\varepsilon_{Hf}(t)$ = −17.9–−34.4) (Dong GC et al., 2013; Shen ZC et al., 2015) of diorite porphyry in the Mujicun Cu-Mo deposit.

The molybdenite Re-Os data in the Mujicun deposit have determined the $^{187}Os/^{188}Os$ ratios with wide variation from −1.3 to 0.3 (Gao YF et al., 2011; Chen C et al., 2013; Dong GC et al., 2013; Shen ZC et al., 2015). These ratios all overlap with the $^{187}Os/^{188}Os$ ratios of crust-derived (0.2–10.0; Barra F et al., 2003) and mantle-derived (0.11–0.15; Meisel T et al., 2001) metals, indicating crust-mantle mixing metallic source for the Mujicun Cu-Mo deposit. In addition, the Re contents in molybdenite from the Mujicun Cu-Mo deposit vary from 23.1×10^{-6} to 469.7×10^{-6}, with an average value of 175.6×10^{-6} (Fig. 9b; Gao YF et al., 2011; Chen C et al., 2013; Dong GC et al., 2013; Shen ZC et al., 2015). The majority of these Re contents are higher than 100×10^{-6} (mantle-derived Mo), only a few Re contents are distributed between 10×10^{-6} and 100×10^{-6} (crust-mantle mixing source of Mo) (Mao JW et al., 1999; Berzina AN et al., 2005), which also suggest crust-mantle mixing Mo source. Considering that the molybdenite often grew with chalcopyrite (Fig. 5), this study further proposes that metallic Cu and Mo in the Mujicun deposit might share a common source. The S-Pb-He-Ar isotopes of sulfides (pyrite, chalcopyrite) in the Mujicun Cu-Mo deposit also indicated major contributions from mantle with limited crustal components for ore-forming fluids and materials (Ma G, 1997; Dong GC et al., 2013; Chen C et al., 2015). The C-H-O-Si isotopes of gangue mineral (quartz, calcite) in the Mujicun deposit show close genetic links with hydrothermal fluid of deep-sourced magma (Ma G, 1997; Qu K, 2012; Dong GC et al., 2013; Chen C et al., 2015). Accordingly, this study concludes that the ore-forming metallic materials of the Mujicun Cu-Mo deposit are derived from crust-mantle mixing source.

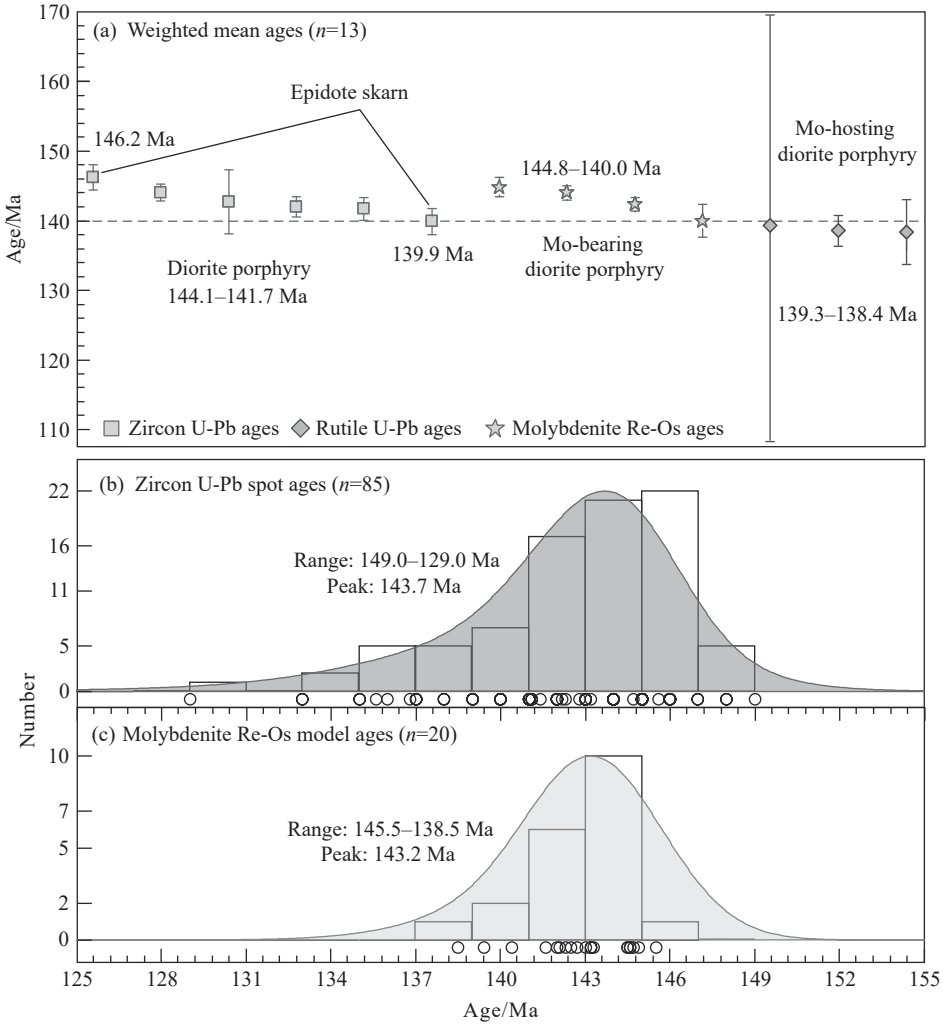

Fig. 8. Different dating age variation diagram (a), histograms of zircon U-Pb spot ages (b), and molybdenite Re-Os model ages (c) of the Mujicun Cu-Mo deposit. Data sources are from Gao YF et al. (2011, 2013); Chen C et al. (2013); Dong GC et al. (2013); Shen ZC et al. (2015).

Previous whole-rock geochemical data of diorite porphyry in the Mujicun Cu-Mo deposit show geochemical affinities related to high-K calc-alkaline I-type granitoids (Dong GC et al., 2013; Qu K et al., 2014), which rules out the magmatic rutile that is formed by the crystallization of high Ti and Fe magma produced by carbonate magma (Cai JH et al., 2008). Thus, this study suggests that the magmatic rutile was generated by the crystallization of high Si, low Fe and Ti magma produced by initial magmatic differentiation (Cai JH et al., 2008). This is also supported by the fractional crystallization of accessory minerals (Fe-Ti oxides, titanite) in diorite porphyry from the Mujicun Cu-Mo deposit (Gao YF et al., 2013). Combined the formation temperatures (574–925°C) of the rutile (Table DR2) and the crystallization temperatures of felsic magma (650–800°C; Larsen ES, 1929), this study further proposes that the fractional crystallization of magmatic rutile might be throughout the whole temperature variation range of dioritic magma. Also, no distinct correlations are shown between Cu/Mo versus ΣREE diagrams (Fig. 9c–d), this study thus indicates that the enrichment degree of REEs in rutile does not covary with the precipitation of Cu and Mo. But a positive correlation is shown between Cu and Mo concentrations (Fig. 9e), which likely results from cogenetic relationship (Fig. 5g–i) and similar precipitation processes during Cu-Mo mineralization. In hydrothermal rutile, several studies identified that orogenic Au deposits are strongly enriched in As and Sb (Agangi A et al., 2019), whereas porphyry Cu deposits only show moderate As and Sb contents (Schirra M and Laurent O, 2021). Although the rutile in the study is magmatic in origin, the As and Sb contents in these rutile are plotted within and close to the field of porphyry Cu deposit (Fig. 9f), which also support the genetic relationship with porphyry Cu mineralization to some extent.

Some studies suggested that the Nb/Ta ratios of continental crust (12–13: Barth MG et al., 2000; Rudnick RL et al., 2003) and depleted mantle (15.5 ± 1.0: Jochum KP et al., 1997) are all lower than chondritic Nb/Ta values (17.5 or 19.9: McDonough WF and Sun SS, 1995; Munker C et al., 2003). Rutile is often enriched in Nb and Ta concentrations, especially the rutile in the remnants of subducted oceanic crust which plays significant role in the balance of Nb/Ta values between continental curst and depleted mantle (McDonough WF, 1991). The Nb/Ta ratios of the rutile in the

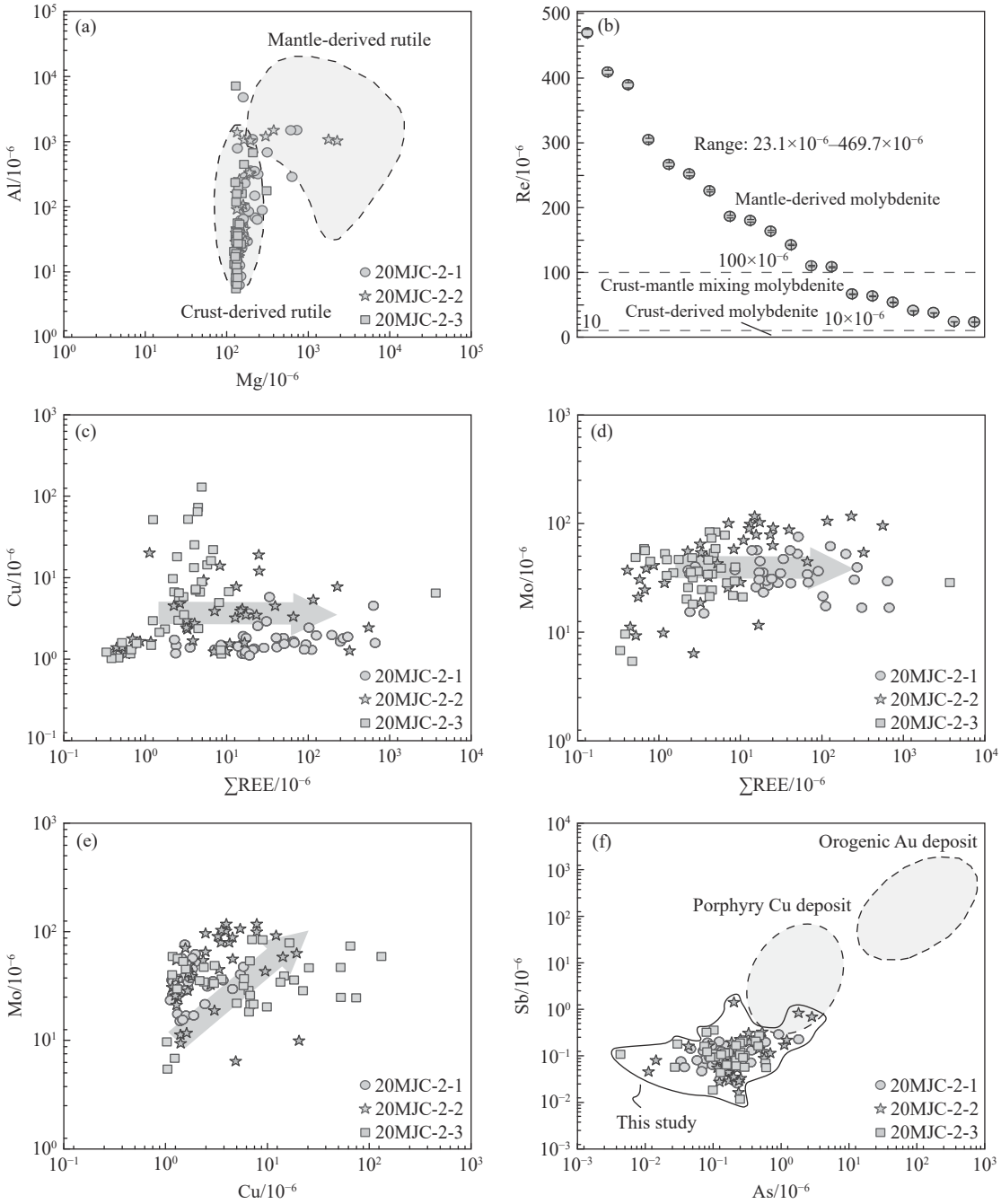

Fig. 9. Variation diagrams of rutile (a, c–f) and molybdenite (b) trace element contents in the Mujicun Cu-Mo deposit. (a) Mg vs. Al diagram (after Smythe D et al., 2008), (b) Re concentrations in molybdenite, (c) ΣREE vs. Cu diagram, (d) ΣREE vs. Mo diagram, (e) Cu vs. Mo diagram, and (f) As vs. Sb diagram (after Agangi A et al., 2019). Molybdenite data sources are from Gao YF et al. (2011); Chen C et al. (2013); Dong GC et al. (2013); Shen ZC et al. (2015).

Mujicun deposit range from 6.28 to 125.55 (n = 115) and can be divided into low (range: 6.28–14.25; mean: 11.33; n = 11), moderate (range: 15.59–19.97; mean: 18.07; n = 10) and high (range: 20.82–125.55; mean: 37.99; n = 94) groups (Table DR2). The majority of the Nb/Ta mean ratios (37.99) are close to residual eclogite, which was produced by the dehydration or partial melting of subducted slabs (33.5 ± 3.5: Kamber BS and Collerson KD, 2000). A few rutile grains show mixed Nb/Ta mean ratios (11.33 and 18.07) of continental crust (12–13: Barth MG et al., 2000; Rudnick RL et al., 2003) and depleted mantle (15.5 ± 1.0: Jochum KP et al., 1997), indicating different degree of crust-mantle magma mixing. Additionally, the subchondritic Nb/Ta values of continental crust and island arc volcanic rocks have been correlated with the melting of subducted slabs in the presence of rutile (Rudnick RL et al., 2000). However, whole-rock geochemical data of diorite porphyry in the Mujicun deposit show geochemical signature of high Sr/Y and La/Yb ratios, which have been ascribed to magmatic evolution and not the partial melting or delamination of thickened lower continental crust (Gao YF et al., 2013), thus excluding arc-related geochemical affinities. Accordingly, the scenario that the

subchondritic Nb/Ta values of continental crust caused by the melting of subducted slabs could be accepted in this study, which further correlated the formation of the Mujicun deposit with subduction-related tectonics.

6.4. Geodynamic implications for the Mujicun Cu-Mo deposit

Mao J et al. (2021a) proposed that the whole eastern Asia underwent a tectonic transition from NW-trending transpression in the Middle-Late Jurassic to Early Cretaceous to EW-trending transtension in the Early-Late Cretaceous within the Paleo-Pacific plate geodynamics. Several major deposits, including porphyry-skarn Cu-Mo-Au deposits, widely developed in the large-scale extensional tectonic setting of the eastern Asia, although most of them are distributed inland from the continental margin for 300–1000 km (Mao J et al., 2021a, 2021b). In eastern China, tectonic regime started to change from compression to extension at about 145 Ma (Li D et al., 2012) and finally transformed into an extensional setting by about 115 Ma (Xue F et al., 2018; Yang F et al., 2019), which is evidenced by numerous A-type Cretaceous granitoids emplaced in the eastern China (Wu FY et al., 2005). Previous study also suggested that the Paleo-Pacific slab was subducted beneath the NCC at a low angle since the Middle Jurassic to the Cretaceous (Zheng Y et al., 2018), followed by slab rollback or retreat at about 144 Ma, resulting in the significant thinning of cratonic mantle at 135–130 Ma (Müller RD et al., 2008; Zheng Y et al., 2018). Further, the peak timing of the extensional setting was constrained at about 125 Ma (Zhu RX et al., 2012a, 2012b), the eastern China, even the whole Eurasian continental margins, was transformed into an active continental margin during the Jurassic to Cretaceous (Wu FY et al., 2011; Sun W et al., 2007; Yang F et al., 2019). The westward subduction of Paleo-Pacific Plate during the Late Mesozoic was considered to have impacted the North Taihang Orogen (Fig. 1a; Zhu L et al., 2009; Zhu RX et al., 2012a; Yang F et al., 2018a, 2018b, 2020a, 2020b). Based on detailed investigations of the Laiyuan intrusive-volcanic complex (Fig. 1b), Xue F et al. (2019, 2021) further confirmed that thermal-mechanical erosion at the central NCC and lithospheric delamination in the eastern NCC were ascribed to the rollback of subducting Paleo-Pacific slab, which resulted in asthenospheric upwelling along the margin of the Trans-North China Orogen (North Taihang Orogen) (Huang XL et al., 2012; Li SR and Santosh M, 2017).

The diorite porphyry and related mineralization of the Mujicun Cu-Mo deposit in the North Taihang Orogen have been suggested to be formed at a lithospheric extensional setting, which is also correlated with lithospheric thinning of the NCC (Gao YF et al., 2011, 2013; Yang F et al., 2019). The heat and crust-mantle mixing material exchange are helpful to the formation of related mineralization in the Taihang Orogen, including the Mujicun Cu-Mo deposit (Dong GC et al., 2013). In addition, the melting of lower crust beneath the Taihang orogen during the Early Cretaceous and related mantle compositions during lithospheric thinning and crust-mantle decoupling also lead to large-scale mineralization in the whole Taihang region (Li SR et al., 2013; Li SR and Santosh M, 2017). In the North Taihang Orogen, except for porphyry Cu-Mo deposits, several skarn Fe-Cu and hydrothermal vein-type Pb-Zn deposits are also widely developed (Fig. 1b). Yang F et al. (2019) determined the emplacement ages of different granitoids from the Zhijiazhuang skarn iron deposit in the North Taihang Orogen at 134–121 Ma, and identified that they were I-type adakitic granites derived from crust-mantle mixing source and correlated with the Paleo-Pacific Plate subduction. Wu JJ et al. (2014) revealed that the ore-forming material sources of Lianbaling Pb-Zn deposit in the North Taihang Orogen were also from crust-mantle mixing components at upper mantle-lower crust. Additionally, numerous skarn iron deposits are widely hosted in the South Taihang Orogen, which were all formed in the Early Cretaceous and linked with dioritic magma and lithospheric thinning of the NCC (Shen ZC et al., 2015; Zhang JQ et al., 2015).

In this study, the rutile U-Pb dating of ore-hosting diorite porphyry defined the ore-forming ages of the Mujicun deposit at 139.3–138.4 Ma. Combined with crust-mantle mixing magma and metallic sources, subduction-related tectonics, and long distance from the continental margin of the eastern NCC, this study proposes that the far-field effect and the rollback of the subducting Paleo-Pacific slab triggered lithospheric extension, asthenosphere upwelling, crust-mantle interaction along with thermo-mechanical erosion during the Early Cretaceous, which jointly resulted in the formation of dioritic magma (Fig. 10; Gao YF et al., 2013; Yang F et al., 2020a; Xue F et al., 2021). Subsequently, the dioritic magmas were shallowly emplaced along NNE-trending ore-controlling faults in intra-continental extensional settings, with concomitant crust-mantle mixing metallic materials to precipitate and finally to generate the Mujicun Cu-Mo deposit in the North Taihang Orogen (Fig. 10).

7. Conclusions

(i) The ore-hosting diorite porphyry yields rutile U-Pb ages of 139.3–138.4 Ma, which constrain the ore-forming age of the Mujicun Cu-Mo deposit in the Early Cretaceous.

(ii) The magma of ore-hosting diorite porphyry and related metallic source in the Mujicun Cu-Mo deposit are all suggested to be derived from the mixture of crust and mantle materials, and the formation of the Mujicun Cu-Mo deposit is correlated with subduction-related tectonics.

(iii) The far-field effect and the rollback of the subducting Paleo-Pacific slab resulted in lithospheric extension, asthenosphere upwelling, crust-mantle interaction, and thermo-mechanical erosion as well as the formation of dioritic magma during the Early Cretaceous. The dioritic magma and crust-mantle mixing metallic materials were subsequently emplaced and precipitated at shallow positions along NNE-trending ore-controlling faults in intra-continental extensional settings to form the Mujicun Cu-Mo deposit.

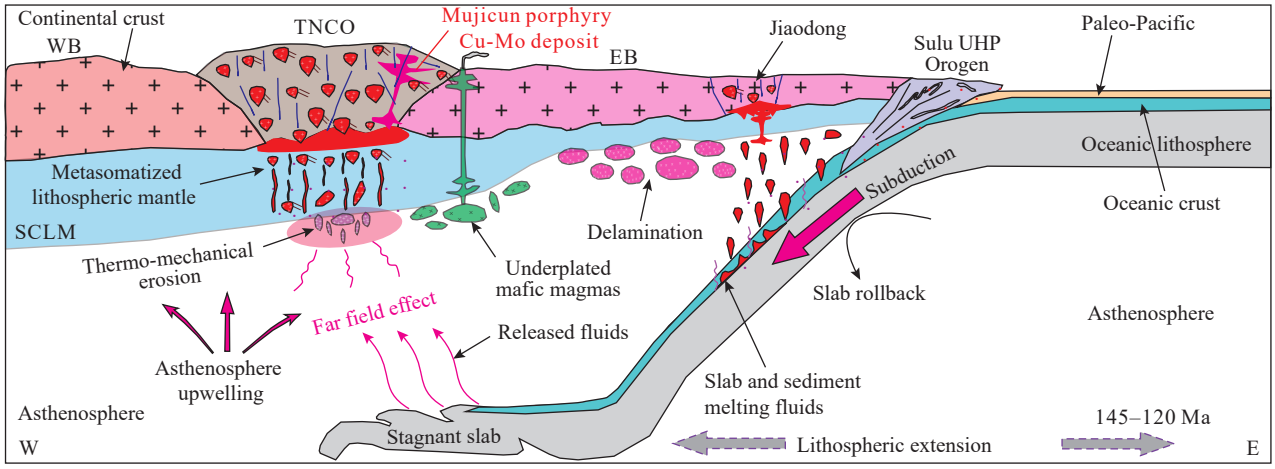

Fig. 10. Schematic tectonic model showing the generation of the Mujicun Cu-Mo deposit in the North China Craton (modified from Yang F et al., 2021b). Abbreviations: WB–Western Block; TNCO–Trans-North China Orogen; EB–Eastern Block; SCLM–Subcontinental lithospheric mantle.

CRediT authorship contribution statement

Fan Yang and Jingwen Mao conceived of the presented idea. Jiarun Tu carried out the experiment. Fan Yang, Siyuan Meng and Zhimin Wang performed the field work. All authors discussed the results and contributed to the final manuscript.

Declaration of competing interest

The authors declare no conflicts of interest.

Acknowledgments

The authors appreciate Prof. Hongying Zhou for her help during rutile U-Pb dating and trace element analysis, and Mr. Zhikuan Chen and Dr. Fei Xue for their assistance related to sample collection. Two anonymous referees are also thanked for their valuable suggestions to improve this paper. This study was jointly supported by the National Natural Science Foundation of China (42202077; 42103025), the Opening Foundation of MNR Key Laboratory of Metallogeny and Mineral Assessment (ZS2209; ZS2106), the Opening Foundation of Key Laboratory of Mineral Resources in Western China (Gansu Province) (MRWCGS-2021-01), the Natural Science Foundation of Gansu Province (22JR5RA440), the Fundamental Research Funds for the Central Universities (LZUJBKY-2022-42), and the Guiding Special Funds of "Double First-Class (First-Class University & First-Class Disciplines)" (561119201) of Lanzhou University, China.

Supplementary dataset

Supplementary data (Tables. DR1–DR2) to this article can be found online at doi: 10.31035/cg2023038.

References

Agangi A, Reddy SM, Plavsa D, Fougerouse D, Clark C, Roberts M, Johnson TE. 2019. Antimony in rutile as a pathfinder for orogenic gold deposits. Ore Geology Reviews, 106, 1–11. doi: 10.1016/j.oregeorev.2019.01.018.

Asadi S, Moore F, Zarasvandi, A. 2014. Discriminating productive and barren porphyry copper deposits in the southeastern part of the central Iranian volcano-plutonic belt, Kerman region, Iran: a review. Earth-Science Reviews, 138, 25–46. doi: 10.1016/j.earscirev.2014.08.001.

Barra F, Ruiz J, Mathur R, Titley S. 2003. A Re-Os study of sulfide minerals from the Bagdad porphyry Cu-Mo deposit, northern Arizona, USA. Mineralium Deposita, 38, 585–596. doi: 10.1007/s00126-002-0341-0.

Barth MG, McDonough WF, Rudnick RL. 2000. Tracking the budget of Nb and Ta in the continental crust. Chemical geology, 165, 197–213. doi: 10.1016/S0009-2541(99)00173-4.

Bertrand G, Guillou-Frottier L, Loiselet C. 2014. Distribution of porphyry copper deposits along the western Tethyan and Andean subduction zones: Insights from a paleotectonic approach. Ore Geology Reviews, 60, 174–190. doi: 10.1016/j.oregeorev.2013.12.015.

Berzina AN, Sotnikov VI, Economou-Eliopoulos M, Eliopoulos DG. 2005. Distribution of rhenium in molybdenite from porphyry Cu-Mo and Mo-Cu deposits of Russia (Siberia) and Mongolia. Ore Geology Reviews, 26, 91–113. doi: 10.1016/j.oregeorev.2004.12.002.

Bibikova E, Skiöld T, Bogdanova S, Gorbatschev R, Slabunov A. 2001. Titanite-rutile thermochronometry across the boundary between the Archaean Craton in Karelia and the Belomorian Mobile Belt, eastern Baltic Shield. Precambrian Research, 105, 315–330. doi: 10.1016/S0301-9268(00)00117-0.

Cai JH, Wang LB, Li JP. 2008. Mineralogical features of rutiles of different modes of occurrence and genetic types and their research significance. Mineral Deposits, 27, 531–538 (in Chinese with English abstract).

Cai JH, Yan GH, Chang GS, Wang XF, Shao HX, Chu ZY. 2003. Petrological and geochemical characteristics of the Wanganzhen complex and discussion on its genesis. Acta Petrologica sinica, 19, 81–92 (in Chinese with English abstract).

Cannell J, Cooke DR, Walshe JL, Stein H. 2005. Geology, mineralization, alteration, and structural evolution of the El Teniente porphyry Cu-Mo deposit. Economic Geology, 100, 979–1003. doi: 10.2113/gsecongeo.100.5.979.

Chen B, Tian W, Zhai M. 2005. Zircon U-Pb geochronology and geochemistry of the Mesozoic magmatism in the Taihang Mountains and other places of the North China craton, with implications for petrogenesis and geodynamic setting. Acta Petrologica Sinica, 21, 13–24 (in Chinese with English abstract).

Chen C, Wang BD, Niu SY, Ma GX, Zhang JZ, Sun AQ, Ma BJ, Chen ZK, Zhang FX, Wang ZL. 2013. Re-Os dating of molybdenite from the Mujicun Cu (-Mo) deposit in Hebei Province and characteristics

of the ore-forming fluids. Geology in China, 40, 1889–1901 (in Chinese with English abstract).
Chen C, Wang BD, Niu SY, Zhang FX, Ma BJ, Zhang JZ, Sun AQ, Wang HT, Ma GX, Chen ZK, Wang ZL. 2015. Discussion on the Ore-forming material sources of Mujicun copper (Molybdenite) polymetallic orefield in Laiyuan County, Hebei Province, China. Journal of Jilin University:Earth Science Edition, 45, 106–118 (in Chinese with English abstract).
Cherniak DJ. 2000. Pb diffusion in rutile. Contributions to Mineralogy and Petrology, 139, 198–207. doi: 10.1007/PL00007671.
Cherniak DJ, Watson EB. 2001. Pb diffusion in zircon. Chemical Geology, 172, 5–24. doi: 10.1016/S0009-2541(00)00233-3.
Clark JR, Williams-Jones AE. 2004. Rutile as a potential indicator mineral for metamorphosed metallic ore deposits. Rapport Final de DIVEX, Sous-projet SC2, Montréal, Canada, 17.
Cluzel D, Aitchison JC, Zhou R, Ireland T, Heizler M, Patias D, Lesimple S, Maurizot P, Teyssier C. 2022. Direct dating of podiform Chromitite: U-Pb (Zircon, Rutile) and $^{40}Ar/^{39}Ar$ (Pargasite) evidence from Tiébaghi Cr deposit (New Caledonia). Ore Geology Reviews, 145, 104873. doi: 10.1016/j.oregeorev.2022.104873.
Dong GC, Santosh M, Li SR, Shen JF, Mo XX, Scott S, Qu K, Wang X. 2013. Mesozoic magmatism and metallogenesis associated with the destruction of the North China Craton: evidence from U–Pb geochronology and stable isotope geochemistry of the Mujicun porphyry Cu-Mo deposit. Ore Geology Reviews, 53, 434–445. doi: 10.1016/j.oregeorev.2013.02.006.
Duan C, Mao J, Xie G, Chen Z, Ma G, Wang Z, Chen T, Li W. 2016. Zircon U-Pb geochronological and Hf isotope study on Tiaojishan volcanic Formation, Mujicun, North Taihang Mountain and implications for regional metallogeny and magmatism. Acta Geologica Sinica, 90, 250–266 (in Chinese with English abstract). doi: 10.1111/1755-6724.13004.
Edwards PM. 2002. Origin 7. 0:scientific graphing and data analysis software. Journal of chemical information and computer sciences, 42, 1270–1271. doi: 10.1021/ci0255432.
Ferry JM, Watson EB. 2007. New thermodynamic models and revised calibrations for the Ti-in-zircon and Zr-in-rutile thermometers. Contributions to Mineralogy and Petrology, 154, 429–437. doi: 10.1007/s00410-007-0201-0.
Gao YF, Santosh M, Wei RH, Ma GX, Chen ZK, Wu JL. 2013. Origin of high Sr/Y magmas from the northern Taihang Mountains: implications for Mesozoic porphyry copper mineralization in the North China Craton. Journal of Asian Earth Sciences, 78, 143–159. doi: 10.1016/j.jseaes.2012.10.040.
Gao YF, Wei RH, Hou ZQ, Ma GX, Zhao RS, Chen ZK, Wu JL, Peng YX, Gao M. 2011. Mujicun porphyry copper mineralization: response to Mesozoic thinning of lithosphere in North China Craton. Mineral Deposits, 30, 890–902 (in Chinese with English abstract).
Hou T, Zhang Z, Keiding JK, Veksler IV. 2015. Petrogenesis of the ultrapotassic Fanshan intrusion in the North China Craton: implications for lithospheric mantle metasomatism and the origin of apatite ores. Journal of Petrology, 56, 893–918. doi: 10.1093/petrology/egv021.
Hou Z, Xiao Y, Shen J, Yu C. 2020. In situ rutile U-Pb dating based on zircon calibration using LA-ICP-MS, geological applications in the Dabie orogen, China. Journal of Asian Earth Sciences, 192, 104261. doi: 10.1016/j.jseaes.2020.104261.
Hou ZQ, Li QY, Gao YF, Lu YJ, Yang ZM, Wang R, Shen ZC. 2015. Lower-crustal magmatic hornblendite in North China Craton: Insight into the genesis of porphyry Cu deposits. Economic Geology, 110, 1879–1904. doi: 10.2113/econgeo.110.7.1879.
Hou ZQ, Ma H, Khin Z, Zhang Y, Wang M, Wang Z, Pan G, Tang R. 2003. The Himalayan Yulong porphyry copper belt: Product of large-scale strike-slip faulting in eastern Tibet. Economic Geology, 98, 125–145. doi: 10.2113/gsecongeo.98.1.125.
Hou ZQ, Yang ZM, Qu XM, Meng XJ, Li ZQ, Beaudoin G, Rui ZY, Gao YF, Zaw K. 2009. The Miocene Gangdese porphyry copper belt generated during post-collisional extension in the Tibetan Orogen. Ore Geology Reviews, 36, 25–51. doi: 10.1016/j.oregeorev.2008.09.006.
Huang XL, Zhong JW, Xu YG. 2012. Two tales of the continental lithospheric mantle prior to the destruction of the North China Craton: Insights from Early Cretaceous mafic intrusions in western Shandong, East China. Geochimica et Cosmochimica Acta, 96, 193–214. doi: 10.1016/j.gca.2012.08.014.
Jochum KP, Pfander J, Snow JE, Hofmann AW. 1997. Nb/Ta in mantle and crust. Eos, 78, 804.
Kamber BS, Collerson KD. 2000. Role of 'hidden' deeply subducted slabs in mantle depletion. Chemical Geology, 166, 241–254. doi: 10.1016/S0009-2541(99)00218-1.
Lan TG, Fan HR, Santosh M, Hu FF, Yang KF, Yang YH, Liu Y. 2012. Early Jurassic high-K calc-alkaline and shoshonitic rocks from the Tongshi intrusive complex, eastern North China Craton: implication for crust–mantle interaction and post-collisional magmatism. Lithos, 140, 183–199. doi: 10.1016/j.lithos.2012.01.015.
Larsen ES. 1929. The temperatures of magmas. American Mineralogist: Journal of Earth and Planetary Materials, 14, 81–94.
Li D, Zhang ST, Yan CH, Wang GW, Song YW, Ma ZB, Han JW. 2012. Late Mesozoic time constraints on tectonic changes of the Luanchuan Mo belt, East Qinling orogen, Central China. Journal of Geodynamics, 61, 94–104. doi: 10.1016/j.jog.2012.02.005.
Li Q, Li S, Zheng YF, Li H, Massonne HJ, Wang Q. 2003. A high precision U-Pb age of metamorphic rutile in coesite-bearing eclogite from the Dabie Mountains in central China: a new constraint on the cooling history. Chemical Geology, 200, 255–265. doi: 10.1016/S0009-2541(03)00194-3.
Li SR, Santosh M. 2017. Geodynamics of heterogeneous gold mineralization in the North China Craton and its relationship to lithospheric destruction. Gondwana Research, 50, 267–292. doi: 10.1016/j.gr.2017.05.007.
Li SR, Santosh M, Zhang HF, Shen JF, Dong GC, Wang JZ, Zhang JQ. 2013. Inhomogeneous lithospheric thinning in the central North China Craton: zircon U-Pb and S-He-Ar isotopic record from magmatism and metallogeny in the Taihang Mountains. Gondwana Research, 23, 141–160. doi: 10.1016/j.gr.2012.02.006.
Li WC, Zhang XF, Yu HJ, Tao D, Liu XL. 2022. Geology and mineralization of the Pulang supergiant porphyry copper deposit (5.11 Mt) in Shangri-la, Yunnan Province, China: A review. China Geology, 5(4), 662–695. doi: 10.31035/cg2022060.
Lin B, Tang JX, Tang P, Zheng WB, Song Y, Li FQ, Leng QF, Wang ZC, Qi J, Sun M, Bello Rodríguez JD. 2023. Geology, geochronology, and exploration of the Jiama giant porphyry copper deposit (11 Mt), Tibet, China: A review. China Geology, 6(2), 338–357. doi: 10.31035/cg2023031.
Liu J, Zhao Y, Liu X, Wang Y, Liu X. 2012. Rapid exhumation of basement rocks along the northern margin of the North China craton in the early Jurassic: Evidence from the Xiabancheng Basin, Yanshan Tectonic Belt. Basin Research, 24, 544–558. doi: 10.1111/j.1365-2117.2011.00538.x.
Ma G. 1997. Geological characteristics and metallogenic model of copper deposit at Muji Village of Laiyuan County, Hebei Province. Journal of Geology and Mineral Resources of North China, 12, 52–66 (in Chinese with English abstract).
Malkovets VG, Rezvukhin DI, Belousova EA, Griffin WL, Sharygin IS, Tretiakova IG, Gibsher AA, O'Reilly SY, Kuzmin DV, Litasov KD, Logvinova AM, Pokhilenke NP, Sobolev NV. 2016. Cr-rich rutile: A powerful tool for diamond exploration. Lithos, 265, 304–311. doi: 10.1016/j.lithos.2016.08.017.
Mao J, Liu P, Goldfarb RJ, Goryachev NA, Pirajno F, Zheng W, Zhou M, Zhao C, Xie G, Yuan S, Liu M. 2021a. Cretaceous large-scale metal accumulation triggered by post-subductional large-scale extension, East Asia. Ore Geology Reviews, 136, 104270. doi: 10.1016/j.oregeorev.2021.104270.
Mao J, Pirajno F, Lehmann B, Luo M, Berzina A. 2014. Distribution of porphyry deposits in the Eurasian continent and their corresponding tectonic settings. Journal of Asian Earth Sciences, 79, 576–584. doi: 10.1016/j.jseaes.2013.09.002.
Mao J, Zheng W, Xie G, Lehmann B, Goldfarb R. 2021b. Recognition of a Middle-Late Jurassic arc-related porphyry copper belt along the southeast China coast: Geological characteristics and metallogenic implications. Geology, 49, 592–596. doi: 10.1130/G48615.1.
Mao JW, Xie GQ, Yuan SD, Liu P, Meng XY, Zhou ZH, Zheng W.

2018. Current research progress and future trends of porphyry-skarn copper and granite-related tin polymetallic deposits in the Circum Pacific metallogenic belts. Acta Petrologica Sinica, 34, 2501–2517 (in Chinese with English abstract).

Mao JW, Zhang Z, Zhang Z, Du A. 1999. Re-Os isotopic dating of molybdenites in the Xiaoliugou W (Mo) deposit in the northern Qilian mountains and its geological significance. Geochimica et Cosmochimica Acta, 63, 1815–1818. doi: 10.1016/S0016-7037(99)00165-9.

McDonough WF. 1991. Partial melting of subducted oceanic crust and isolation of its residual eclogitic lithology. Philosophical Transactions of the Royal Society of London. Series A:Physical and Engineering Sciences, 335, 407–418. doi: 10.1098/rsta.1991.0055.

McDonough WF, Sun SS. 1995. The composition of the Earth. Chemical geology, 120, 223–253. doi: 10.1016/0009-2541(94)00140-4.

Meinhold G. 2010. Rutile and its applications in earth sciences. Earth-Science Reviews, 102, 1–28. doi: 10.1016/j.earscirev.2010.06.001.

Meisel T, Walker RJ, Irving AJ, Lorand JP. 2001. Osmium isotopic compositions of mantle xenoliths: a global perspective. Geochimica et Cosmochimica Acta, 65, 1311–1323. doi: 10.1016/S0016-7037(00)00566-4.

Mezger K, Hanson GN, Bohlen SR. 1989. High-precision U-Pb ages of metamorphic rutile: application to the cooling history of high-grade terranes. Earth and Planetary Science Letters, 96, 106–118. doi: 10.1016/0012-821X(89)90126-X.

Munker C, Pfander JA, Weyer S, Buchl A, Kleine T, Mezger K. 2003. Evolution of planetary cores and the Earth-Moon system from Nb/Ta systematics. Science, 301, 84–87. doi: 10.1126/science.108466.

Müller RD, Sdrolias M, Gaina C, Steinberger B, Heine C. 2008. Long-term sea-level fluctuations driven by ocean basin dynamics. Science, 319, 1357–1362. doi: 10.1126/science.1151540.

Pearce NJ, Perkins WT, Westgate JA, Gorton MP, Jackson SE, Neal CR, Chenery SP. 1997. A compilation of new and published major and trace element data for NIST SRM 610 and NIST SRM 612 glass reference materials. Geostandards newsletter, 21, 115–144. doi: 10.1111/j.1751-908X.1997.tb00538.x.

Pi QH, Hu RZ, Xiong B, Li QL, Zhong RC. 2017. In situ SIMS U-Pb dating of hydrothermal rutile: reliable age for the Zhesang Carlin-type gold deposit in the golden triangle region, SW China. Mineralium Deposita. 52, 1179–1190. doi: 10.1007/s00126-017-0715-y

Porter JK, McNaughton NJ, Evans NJ, McDonald BJ. 2020. Rutile as a pathfinder for metals exploration. Ore Geology Reviews, 120, 103406. doi: 10.1016/j.oregeorev.2020.103406.

Qu K. 2012. Geology and mineralization in Mujicun porphyry Cu-Mo deposit, Northern Taihang Mt., China. China University of Geosciences (Beijing), Master thesis, 1–78 (in Chinese with English abstract).

Qu K, Dong GC, Li SR, Shen JF, Wang YJ, Wang X, Luo W. 2014. Lithogeochemistry and Sr-Nd-Pb isotopic characteristics of Mujicun porphyry Cu-Mo deposit in Taihang Mountains and their significance. Geoscience, 28, 449–460 (in Chinese with English abstract).

Rabbia OM, Hernández LB, French DH, King RW, Ayers JC. 2009. The El Teniente porphyry Cu-Mo deposit from a hydrothermal rutile perspective. Mineralium Deposita, 44, 849–866. doi: 10.1007/s00126-009-0252-4.

Richards JP. 2022. Porphyry copper deposit formation in arcs: What are the odds? Geosphere, 18, 130–155. doi: 10.1130/GES02086.1

Rudnick RL, Barth M, Horn I, McDonough WF. 2000. Rutile-bearing refractory eclogites: missing link between continents and depleted mantle. Science, 287, 278–281. doi: 10.1126/science.287.5451.278.

Rudnick RL, Gao S, Holland HD, Turekian KK. 2003. Composition of the continental crust. The crust, 3, 1–64.

Rui ZY, Hou ZQ, Qu XM, Zhang LS, Wang LS, Liu YL. 2003. Metallogenetic epoch of Gangdese porphyry copper belt and uplift of Qinghai-Tibet plateau. Mineral Deposits, 22, 217–225 (in Chinese with English abstract).

Schirra M, Laurent O. 2021. Petrochronology of hydrothermal rutile in mineralized porphyry Cu systems. Chemical Geology, 581, 120407. doi: 10.1016/j.chemgeo.2021.120407.

Schmidt MW, Dardon A, Chazot G, Vannucci R. 2004. The dependence of Nb and Ta rutile-melt partitioning on melt composition and Nb/Ta fractionation during subduction processes. Earth and Planetary Science Letters, 226, 415–432. doi: 10.1016/j.epsl.2004.08.010.

Scott KM. 2005. Rutile geochemistry as a guide to porphyry Cu-Au mineralization, Northparkes, new South Wales, Australia. Geochemistry: Exploration, Environment, Analysis, 5, 247–253. doi: 10.1144/1467-7873/03-055.

Scott KM, Radford NW. 2007. Rutile compositions at the Big Bell Au deposit as a guide for exploration. Geochemistry:Exploration, Environment, Analysis,7,353–361. doi: 10.1144/1467-7873/07-135.

Shen JF, Li SR, Santosh M, Dong GC, Wang YJ, Liu HM, Peng ZD, Zhang ZY. 2015. Zircon U-Pb geochronology of the basement rocks and dioritic intrusion associated with the Fushan skarn iron deposit, southern Taihang Mountains, China. Journal of Asian Earth Sciences, 113, 1132–1142. doi: 10.1016/j.jseaes.2015.01.009.

Shen ZC, Hou ZQ, Chen ZK, Li QY, Zhou YM, Wang ZM. 2015. Molybdenite Re-Os isotopic dating and zircon SHRIMP U-Pb and Hf isotopic compositions of the Mujicun porphyry deposit. Acta Petrologica et Mineralogica, 34, 526–538 (in Chinese with English abstract).

Sillitoe RH. 1972. A plate tectonic model for the origin of porphyry copper deposits. Economic Geology, 67, 184–197. doi: 10.2113/gsecongeo.67.2.184.

Sillitoe RH. 2010. Porphyry copper systems. Economic Geology, 105, 3–41. doi: 10.2113/gsecongeo.105.1.3.

Smythe D, Schulze D, Brenan J. 2008. Rutile as a kimberlite indicator mineral: minor and trace element geochemistry. In International Kimberlite Conference: Extended Abstracts (Vol. 9).

Sobolev NV, Yefimova ES. 2000. Composition and petrogenesis of Ti-oxides associated with diamonds. International Geology Review, 42, 758–767. doi: 10.1080/00206810009465110.

Sun SS, McDonough WF. 1989. Chemical and isotopic systematics of oceanic basalts: implications for mantle composition and processes. Geological Society, London, Special Publications, 42, 313–345. doi: 10.1144/GSL.SP.1989.042.01.19

Sun W, Ding X, Hu YH, Li XH. 2007. The golden transformation of the Cretaceous plate subduction in the west Pacific. Earth and Planetary Science Letters, 262, 533–542. doi: 10.1016/j.epsl.2007.08.021.

Suzuki K, Shimizu H, Masuda A. 1996. Re-Os dating of molybdenites from ore deposits in Japan: Implication for the closure temperature of the Re-Os system for molybdenite and the cooling history of molybdenum ore deposits. Geochimica et Cosmochimica Acta, 60, 3151–3159. doi: 10.1016/0016-7037(96)00164-0.

Tang M, Lee CTA, Chen K, Erdman M, Costin G, Jiang H. 2019. Nb/Ta systematics in arc magma differentiation and the role of arclogites in continent formation. Nature Communications, 10, 1–8. doi: 10.1038/s41467-018-08198-3.

Vermeesch P. 2018. IsoplotR: a free and open toolbox for geochronology. Geoscience Frontiers, 9, 1479–1493. doi: 10.1016/j.gsf.2018.04.001.

Vry JK, Baker JA. 2006. LA-MC-ICPMS Pb-Pb dating of rutile from slowly cooled granulites: confirmation of the high closure temperature for Pb diffusion in rutile. Geochimica et Cosmochimica Acta, 70, 1807–1820. doi: 10.1016/j.gca.2005.12.006.

Wang Y, Li H. 2008. Initial formation and Mesozoic tectonic exhumation of an intracontinental tectonic belt of the northern part of the Taihang Mountain belt, eastern Asia. The Journal of Geology, 116, 155–172. doi: 10.1086/529153.

Watson EB, Wark DA, Thomas JB. 2006. Crystallization thermometers for zircon and rutile. Contributions to Mineralogy and Petrology, 151, 413–433. doi: 10.1007/s00410-006-0068-5.

Wu FY, Han RH, Yang JH, Wilde SA, Zhai MG, Park SC. 2007. Initial constraints on the timing of granitic magmatism in North Korea using U–Pb zircon geochronology. Chemical Geology, 238, 232–248. doi: 10.1016/j.chemgeo.2006.11.012.

Wu FY, Lin JQ, Wilde SA, Yang JH. 2005. Nature and significance of the Early Cretaceous giant igneous event in eastern China. Earth and Planetary Science Letters, 233, 103–119. doi: 10.1016/j.epsl.2005.02.019.

Wu FY, Sun DY, Ge WC, Zhang YB, Grant ML, Wilde SA, Jahn BM. 2011. Geochronology of the Phanerozoic granitoids in northeastern

China. Journal of Asian Earth Sciences, 41, 1–30. doi: 10.1016/j.jseaes.2010.11.014.

Wu JJ, Liu JC, Zhang HD, Hou LM, Zheng LH. 2014. Geological characteristics and their ore-forming material sources of Lianbaling Pb-Zn deposit in Taihang Mountains. Journal of Earth Sciences & Environment, 36 (in Chinese with English abstract).

Xiao W, Li S, Santosh M, Jahn BM. 2012. Orogenic belts in Central Asia: Correlations and connections. Journal of Asian Earth Sciences, 49, 1–6. doi: 10.1016/j.jseaes.2012.03.001.

Xiao X, Zhou T, White NC, Fan Y, Zhang L, Chen X. 2021. Porphyry Cu mineralization processes of Xinqiao deposit, Tongling ore district: Constraints from the geochronology and geochemistry of zircon, apatite, and rutile. Ore Geology Reviews, 138, 104340. doi: 10.1016/j.oregeorev.2021.104340.

Xiao Y, Sun W, Hoefs J, Simon K, Zhang Z, Li S, Hofmann AW. 2006. Making continental crust through slab melting: constraints from niobium-tantalum fractionation in UHP metamorphic rutile. Geochimica et Cosmochimica Acta, 70, 4770–4782. doi: 10.1016/j.gca.2006.07.010.

Xiao YL, Huang J, Liu L, Li DY. 2011. Rutile, an important "reservoir" for geochemical information. Acta Petrolagica Sinica, 27, 398–416 (in Chinese with English abstract).

Xue F, Santosh M, Kim SW, Tsunogae T, Yang F. 2021. Thermo-mechanical destruction of Archean cratonic roots: Insights from the Mesozoic Laiyuan granitoid complex, North China Craton. Lithos, 400, 106394. doi: 10.1016/j.lithos.2021.106394.

Xue F, Santosh M, Tsunogae T, Yang F. 2019. Geochemical and isotopic imprints of early cretaceous mafic and felsic dyke suites track lithosphere-asthenosphere interaction and craton destruction in the North China Craton. Lithos, 326, 174–199. doi: 10.1016/j.lithos.2018.12.013.

Xue F, Wang G, Santosh M, Yang F, Shen Z, Kong L, Guo N, Zhang X, Jia, W. 2018. Geochemistry and geochronology of ore-bearing and barren intrusions in the Luanchuan ore fields of East Qinling metallogenic belt, China: diverse tectonic evolution and implications for mineral exploration. Journal of Asian Earth Sciences, 157, 57–77. doi: 10.1016/j.jseaes.2017.04.027.

Yang J, Wu F. 2009. Triassic magmatism and its relation to decratonization in the eastern North China Craton. Science in China Series D:Earth Sciences, 52, 1319–1330. doi: 10.1007/s11430-009-0137-5.

Yang F, Kim SW, Tsunogae T, Zhou H. 2021b. Multiple enrichment of subcontinental lithospheric mantle with Archean to Mesozoic components: Evidence from the Chicheng ultramafic complex, North China Craton. Gondwana Research, 94, 201–221. doi: 10.1016/j.gr.2021.03.005.

Yang F, Santosh M, Glorie S, Jepson G, Xue F, Kim SW. 2020b. Meso-Cenozoic multiple exhumation in the Shandong Peninsula, eastern North China Craton: Implications for lithospheric destruction. Lithos, 370, 105597. doi: 10.1016/j.lithos.2020.105597.

Yang F, Santosh M, Kim SW. 2018a. Mesozoic magmatism in the eastern North China Craton: Insights on tectonic cycles associated with progressive craton destruction. Gondwana Research, 60, 153–178. doi: 10.1016/j.gr.2018.04.003.

Yang F, Santosh M, Kim SW, Zhou H. 2021a. Late Neoarchean to Paleoproterozoic arc magmatism in the Shandong Peninsula, North China Craton and its tectonic implications. Precambrian Research, 358, 106188. doi: 10.1016/j.precamres.2021.106188.

Yang F, Santosh M, Kim SW, Zhou H, Jeong YJ. 2020a. Late Mesozoic intraplate rhyolitic volcanism in the North China Craton: Far-field effect of the westward subduction of the Paleo-Pacific Plate. GSA Bulletin, 132, 291–309. doi: 10.1130/B35123.1.

Yang F, Santosh M, Kim SW, Zhou H, Xue F. 2019. Early Cretaceous adakitic granitoids from the Zhijiazhuang skarn iron deposit, North Taihang Mountain, China: Implications for petrogenesis and metallogenesis associated with craton destruction. Geological Journal, 54, 3189–3211. doi: 10.1002/gj.3320.

Yang F, Santosh M, Tang L. 2018b. Extensive crustal melting during craton destruction: evidence from the Mesozoic magmatic suite of Junan, eastern North China Craton. Journal of Asian Earth Sciences, 157, 119–140. doi: 10.1016/j.jseaes.2017.07.010.

Yang HH, Wang Q, Li YB, Lin B, Song Y, Wang YY, He W, Li HW, Li S, Li JL, Liu CC, Feng SB, Xin T, Fu XL, Liang XJ, Zhang Q, Wang BQ, Li Y. 2022. Geology and mineralization of the Tiegelongnan supergiant porphyry-epithermal Cu (Au, Ag) deposit (10 Mt) in western Tibet, China: A review. China Geology, 5(1), 136–159. doi: 10.31035/cg2022001.

Yang ZM, Goldfarb R, Chang ZS. 2016. Generation of postcollisional porphyry copper deposits in southern Tibet triggered by subduction of the Indian continental plate. Society of Economic Geologists Special Publication, 19, 279–300. doi: 10.5382/SP.19.11.

Zack TV, Moraes RD, Kronz A. 2004a. Temperature dependence of Zr in rutile: empirical calibration of a rutile thermometer. Contributions to Mineralogy and Petrology, 148, 471–488. doi: 10.1007/s00410-004-0617-8.

Zack TV, Von Eynatten H, Kronz A. 2004b. Rutile geochemistry and its potential use in quantitative provenance studies. Sedimentary Geology, 171, 37–58. doi: 10.1016/j.sedgeo.2004.05.009.

Zhai MG, Santosh M. 2011. The early Precambrian odyssey of the North China Craton: a synoptic overview. Gondwana Research, 20, 6–25. doi: 10.1016/j.gr.2011.02.005.

Zhang JQ, Li SR, Santosh M, Wang JZ, Li Q. 2015. Mineral chemistry of high-Mg diorites and skarn in the Han-Xing Iron deposits of South Taihang Mountains, China: Constraints on mineralization process. Ore Geology Reviews, 64, 200–214. doi: 10.1016/j.oregeorev.2014.07.007.

Zhang HD, Liu JC, Wang JY, Zhang SN, Hu B, Wang DQ, Han S. 2016. Petrology, geochronology and geochemistry characteristics of Wang' anzhen complex in the northern Taihang Mountain and their geological significance. Acta Petrologica Sinica, 32, 727–745 (in Chinese with English abstract).

Zhang L, Wu JL, Tu JR, Wu D, Li N, Xia XP, Ren ZY. 2020. RMJG Rutile: A New Natural Reference Material for Microbeam U-Pb Dating and Hf Isotopic Analysis. Geostandards and Geoanalytical Research, 44, 133–145. doi: 10.1111/ggr.12304.

Zhang SH, Zhao Y, Davis GA, Ye H, Wu F. 2014. Temporal and spatial variations of Mesozoic magmatism and deformation in the North China Craton: Implications for lithospheric thinning and decratonization. Earth-Science Reviews, 131, 49–87. doi: 10.1016/j.earscirev.2013.12.004.

Zhang S, Ju N, Zhang GB, Zhao YD, Ren YS, Liu BS, Wang H, Guo RR, Yang Q, Sun ZM, Xu FM, Wang KY, Hao YJ. 2023. Geology and mineralization of the Duobaoshan supergiant porphyry Cu-Au-Mo-Ag deposit (2.36 Mt) in Heilongjiang Province, China: A review. China Geology, 6(1), 100–136. doi: 10.31035/cg2023006.

Zhao G, Sun M, Wilde SA, Li S. 2005. Late Archean to Paleoproterozoic evolution of the North China Craton: key issues revisited. Precambrian Research, 136, 177–202. doi: 10.1016/j.precamres.2004.10.002.

Zhao G, Zhai M. 2013. Lithotectonic elements of Precambrian basement in the North China Craton: review and tectonic implications. Gondwana Research, 23, 1207–1240. doi: 10.1016/j.gr.2012.08.016.

Zheng Y, Xu Z, Zhao Z, Dai L. 2018. Mesozoic mafic magmatism in North China: Implications for thinning and destruction of cratonic lithosphere. Science China Earth Sciences, 61, 353–385. doi: 10.1007/s11430-017-9160-3.

Zheng YF, Gao XY, Chen RX, Gao T. 2011. Zr-in-rutile thermometry of eclogite in the Dabie orogen: Constraints on rutile growth during continental subduction-zone metamorphism. Journal of Asian Earth Sciences, 40, 427–451. doi: 10.1016/j.jseaes.2010.09.008.

Zhou HY, Li HK, Cui YR, Geng JZ, Zhang J, Li HM. 2013. Rutile U-Pb isotopic dating methodology. Acta Geologica Sinica, 87, 1439–1446 (in Chinese with English abstract).

Zhu L, Zhang G, Guo B, Lee B. 2009. He-Ar isotopic system of fluid inclusions in pyrite from the molybdenum deposits in south margin of North China Block and its trace to metallogenetic and geodynamic background. Chinese Science Bulletin, 54, 2479–2492. doi: 10.1007/s11434-009-0047-0.

Zhu RX, Xu Y, Zhu G, Zhang H, Xia Q, Zheng T. 2012a. Destruction of the north China Craton. Science China Earth Sciences, 55, 1565–1587. doi: 10.1007/s11430-012-4516-y.

Zhu RX, Yang JH, Wu FY. 2012b. Timing of destruction of the North China Craton. Lithos, 149, 51–60. doi: 10.1016/j.lithos.2012.05.013.